Monthly Notices of the ROYAL ASTRONOMICAL SOCIETY

MNRAS **542,** 2184–2210 (2025) https://doi.org/10.1093/mnras/staf1181
Advance Access publication 2025 July 31

Quantifying when and where strong magnetic skew forms in a data-driven global non-potential model of the solar corona I: production and persistence of skew

J. Reid ,[1]★ D. H. Mackay[1] and L. A. Upton[2]

[1]*School of Mathematics and Statistics, University of St Andrews, St Andrews, Fife KY16 9SS, UK*
[2]*SouthWest Research Institute, 1301 Walnut Street, Suite 400, Boulder, CO 80302, USA*

Accepted 2025 July 14. Received 2025 June 21; in original form 2024 October 16

ABSTRACT

Strong magnetic skew characterizes several non-potential structures in the solar corona, including filaments, which can erupt, producing major geomagnetic effects. Magnetic skew is thus a useful property in understanding locations of free magnetic energy in, and making forecasts from, global coronal magnetic field models. We develop a new technique for analysing the formation, evolution, and persistence of magnetic skew systematically in such models. This technique is applied to data-constrained magnetofrictional simulations, which include flux emergence in magnetic bipolar regions as observed on the Sun. Magnetic skew in the model is analysed, both globally and within the Earth-bound field of view. The latter is considered as these simulations have an observational bias: magnetogram observations can only be made along the Sun–Earth line. Results show that small patches of strong skew form incrementally, especially around recently emerged bipolar regions. However, large areas of strong skew, of sizes typical of filaments, take approximately two weeks to form after the emergence of new flux. Because of this observational bias in including new bipolar regions, most areas of strong skew in the model form on the far side of the Sun. Once formed, these areas may persist over long periods of time, comparable with the time-scale for solar rotation, and reproduce long-lived solar phenomena. Therefore, most strongly skewed regions in the model on the Earth-facing side of the Sun rotate into the field of view and do not form there. This illustrates a limitation of any global data-driven model that dynamically builds non-potentiality and skew through surface motions and flux emergence, with emergence based solely on observations from the Sun–Earth line.

Key words: magnetohydrodynamics (MHD) – methods: numerical – Sun: atmosphere – Sun: filaments, prominences – Sun: magnetic fields.

1 INTRODUCTION

Solar filaments are extensive features appearing on the Sun, typically seen in H α absorption over the solar disc. For historical reasons, they are often referred to as prominences when viewed at the limb. Filaments contain cool dense plasma, suspended in the corona against the action of gravity by their magnetic fields (Parenti 2014). Although they often persist stably for long periods of time, filaments are liable to erupt, consequently launching coronal mass ejections (CMEs). On average, one such ejection from the Sun takes place every day. Of these, two-thirds are associated with erupting prominences (Golub & Pasachoff 1997). Such events have long been documented for their ability to cause geomagnetic disturbances at Earth (e.g. Sabine 1852; Hale 1931; Newton 1943; McLean 1959), in a phenomenon known as 'space weather' (in the term coined by Davis 1957, 1959). Space weather has grown in strategic importance in recent years, and has been listed on the British National Risk Register (Hapgood et al. 2021).

Filaments lie above polarity inversion lines (PILs; Babcock & Babcock 1955) within filament channels. Filament channels are regions characterized by fibrils antiparallel on either side of PILs, although not all filament channels contain a filament (Martin 1998). In a filament or a filament channel, the component of the magnetic field along its long axis is dominant (Foukal 1971) and the magnetic field is strongly skewed (Leroy, Bommier & Sahal-Brechot 1983, 1984) relative to a normal to the underlying photospheric PIL. Magnetic skew is thus a useful indicator of where filaments can form, of the storage of free non-potential magnetic energy, and of where eruptions may occur.

With the growth and development of computational resources, numerical modelling of the solar magnetic field has become increasingly refined and increasingly able to probe the formation of filaments, along with other phenomena. Early models treat the coronal and photospheric magnetic fields entirely independently (e.g. Altschuler & Newkirk 1969). More advanced models (beginning with van Ballegooijen, Cartledge & Priest 1998; van Ballegooijen, Priest & Mackay 2000) begin to couple the evolution of the photospheric and coronal fields, accounting for their interaction and for the influence of the former upon the latter.

At the same time as treating this coupling of coronal and photospheric systems, it is equally important over time to consider the evolving photospheric input of new magnetic flux into this global magnetic system. Early models (e.g. Mackay, Gaizauskas & van

★ E-mail: jr93@st-andrews.ac.uk

Ballegooijen 2000) start from a given set of initial conditions and allow the magnetic field to evolve according to known governing equations, without accounting for the continual supply of new flux into the global field through the photospheric boundary. As with any physical system, the evolution of the global magnetic field is a product both of its internal physics, and of the external influences upon the system, which constitute the boundary conditions for models. Recognizing this, simulations such as those of Yeates, Mackay & van Ballegooijen (2007) start treating the emergence of flux in the form of idealized bipolar regions, showing the importance of this process for the accuracy of the model (Yeates et al. 2007, 2008). Including this flux, however, requires observational data to prescribe the properties of bipolar regions to be inserted into the simulations.

When new bipolar regions emerge on the photosphere, they create new PILs and bring new flux into the solar atmosphere. As this new flux interacts with the pre-existing field and is acted upon by motions on the surface, magnetic shear or skew can form along the PILs, hence the importance of including new magnetic flux when modelling the formation of filaments. Using magnetograms produced by instruments such as the Helioseismic and Magnetic Imager (HMI; Scherrer et al. 2012) aboard the Solar Dynamics Observatory (Pesnell, Thompson & Chamberlin 2012), the emergence of these regions is detectable. Having identified the emergence of new flux, the results can be used in a data-constrained simulation of the coronal magnetic field to provide the lower boundary condition. In such a simulation, the coronal magnetic field evolves in response to the emerging flux, among other factors such as surface motions and supergranular diffusion. One limitation that such data-constrained simulations suffer is that bipolar regions can only be observed and their properties determined, for insertion into a simulation, within the Earth-bound field of view. This extends approximately 60° on either side of central meridian as seen from Earth.[1] For this reason, it is important to quantify how this limited field of view affects the production of strong magnetic skew in data-constrained simulations.

Yeates et al. (2018) compare several competing data-driven simulations, seeking numerically to reproduce the state of the solar magnetic field at the time of the total solar eclipse on 2015 March 20. In particular, the magnetofrictional model of the global coronal field (as originated by Mackay & van Ballegooijen 2006a; Yeates 2014) is compared with non-linear force-free (Wiegelmann 2007; Amari et al. 2013), magnetohydrostatic (Bogdan & Low 1986), force-free electrodynamic (Contopoulos, Kalapotharakos & Georgoulis 2011), and magnetohydrodynamic (Mikic & Linker 1994; Feng et al. 2012) models. In that comparison, an isolated example of the magnetofrictional model, with one particular parameter regime, one initial condition, and one set of boundary conditions, is used.

Expanding upon that, Mackay & Upton (2022) demonstrate the full capability of the magnetofrictional model, and the wide range of physical parameters available, including comparing two data sets containing bipolar regions. First, they use a set produced from synoptic magnetograms, with data from HMI, produced every Carrington rotation. Secondly, a data set is inferred from an Advective Flux Transport (AFT; Upton & Hathaway 2014a, b) simulation, which is itself informed by normal-component HMI magnetograms, but which additionally incorporates surface flux transport (SFT) in order to provide global magnetic field maps that vary across all longitudes every day. Data at higher cadence[2] available in the latter set, combined with allowing bipolar regions to emerge both pre- and post-central meridian, yield considerably different evolutions in the magnetic energy, the electric current, and both the amount and the distribution of open flux, compared with the results from using the synoptic data. All of these are important for the behaviour of the solar wind, which can, in turn, exert geomagnetic effects.

Since the primary intention of the work of Mackay & Upton (2022) is not to focus upon the production and persistence of strongly skewed magnetic fields, it is pertinent to focus more narrowly upon these issues in this work. In order to do so, new techniques are developed and presented, which allow for the identification and quantification of the formation of skew in the global magnetofrictional model. In addition, the persistence of skew in the coronal magnetic field in the global magnetofrictional model after it has formed from one solar rotation to the next can be studied. Once developed, these techniques are applied, both over the entire Sun and specifically within the limited field of view from Earth. By doing so, it is possible to consider how the limited range of longitudes over which bipolar regions are inserted affects the production of skew at longitudes visible from Earth.

Starting from observations of the Sun's photospheric magnetic field on 2014 September 1, numerical simulations of the coupled photospheric and coronal fields are undertaken in order to follow the evolution of the coronal field in the period up to 2015 March 30. In the simulations presented here, skew in the magnetic field is identified and calculated over the full duration of the simulations.

In Section 2, the model used for simulating the global magnetic field is outlined, alongside the method for identifying bipolar regions from observations. Overall aspects of the coronal magnetic evolution in the simulations are described in Section 3. Then, Section 4 discusses their implications for the evolution of skew within the solar corona on a macroscopic scale, both over the whole Sun and within the field of view seen from Earth. Section 5 provides a more detailed discussion of the formation and evolution of individual distinct features characterized by strong magnetic skew. Section 6 demonstrates an approach for the systematic detection of such features of strong skew within the Earth-bound field of view. As an illustration of the processes and time-scales typically involved in the generation of skew, Section 7 treats the case of a particularly notable filament, which is within the Earth-bound field of view at the time of the total solar eclipse of 2015 March 20. Section 8 statistically considers the time-scale for the generation of skew in the magnetic field relative to the emergence of flux in the global magnetofrictional model. Finally, Section 9 reviews some of the major conclusions, and considers future implications of the work.

2 METHOD

2.1 Global simulations

Numerical simulations of the coronal magnetic field are performed according to the non-potential evolutionary model originated by Mackay & van Ballegooijen (2006a) and Yeates (2014), which has successfully been used to study the hemispheric pattern in chirality of filaments (Yeates et al. 2008), open flux (Yeates et al. 2010), flux ropes (Yeates & Mackay 2009), and CMEs (Pagano, Mackay & Poedts 2013, 2014). Mackay, DeVore & Antiochos (2014) provide

[1] While half of the Sun's surface, up to 90° on either side of central meridian, can be seen from Earth at any one time, reliable measurements cannot be taken at or close to the limb as a result of projection effects. Here, measurements are deemed to be reliable of locations within 60° of central meridian, and this window is taken to be the 'Earth-bound field of view'.

[2] AFT maps are available at a cadence up to one map every 15 min.

fuller details of the operation of the numerical code implementing this method, which is briefly outlined here.

Defined in terms of a magnetic vector potential $\vec{A}$, the magnetic field,

$$\vec{B}(r, \theta, \phi, t) = \nabla \times \vec{A}, \tag{1}$$

evolves within a domain,

$$(r, \theta, \phi) \in [R_\odot, 2.5R_\odot] \times [0, \pi] \times [0, 2\pi], \tag{2}$$

defined in spherical polar coordinates. In longitude, the grid has cells of uniform width $\Delta = 0.46875^\circ$. In latitude, the grid is stretched, with cells having width Δ at the equator, reducing towards the poles. Within the code, the spherical coordinates are transformed into modified coordinates x, y, z for computation:

$$x = \frac{\phi}{\Delta} \tag{3a}$$

$$y = -\frac{\log \tan \frac{\theta}{2}}{\Delta} \tag{3b}$$

$$z = \frac{\log \frac{r}{R_\odot}}{\Delta}, \tag{3c}$$

where $R_\odot$ is the solar radius. Two distinct parts constitute the global model, namely those representing the photospheric and the coronal magnetic fields, which are coupled and evolve simultaneously.

First, in the photosphere, where the plasma-β is high, fluid forces dominate over magnetic, and the very low resistivity leaves the magnetic field largely 'frozen' to the plasma. Photospheric motions, responsible for SFT, therefore heavily influence the magnetic evolution. In particular, three processes contribute. First is differential rotation, whereby different latitudes rotate at different rates, which is treated using the profile (from Snodgrass 1983):

$$\Omega(\theta) = \left(0.18 - 2.3\cos^2\theta - 1.62\cos^4\theta\right) \deg \mathrm{d}^{-1}. \tag{4}$$

Secondly, the poleward drift of meridional flow is modelled (following Schüssler & Baumann 2006) by a latitudinal velocity:

$$u_\theta = -15 \sin 2\lambda e^{\pi - 2|\lambda|} \,\mathrm{m\,s^{-1}}, \tag{5}$$

where λ is latitude, given by $\lambda = 90^\circ - \theta$. Finally, surface diffusion, representing the large-scale consequence of smaller scale supergranular flows, is treated through a regular second-order diffusion operator (as proposed by Leighton 1964), with coefficient (from DeVore et al. 1985):

$$D = 450 \,\mathrm{km^2\,s^{-1}}. \tag{6}$$

All three are applied in order to prescribe the boundary flows $\vec{v}_s$ and diffusion on the solar surface. In conjunction with the emergence of flux in the form of bipolar regions ($\vec{S}_b$), these processes govern the evolution of the photospheric magnetic flux:

$$\frac{\partial \vec{A}_s}{\partial t} = \vec{v}_s \times \vec{B}_r - D\nabla_s \times \vec{B}_r + \vec{S}_b. \tag{7}$$

In the second, coronal part of the model, the magnetic potential evolves according to

$$\frac{\partial \vec{A}}{\partial t} = \vec{v} \times \vec{B} + \vec{R}, \tag{8}$$

where the velocity is given by

$$\vec{v} = \frac{1}{\nu}\frac{\vec{j} \times \vec{B}}{|\vec{B}|^2} + v_0 e^{-\frac{2.5R_\odot - r}{r_w}} \vec{e}_r, \tag{9}$$

where $\vec{j} = \nabla \times \vec{B}$. This velocity is the combination of, respectively, a magnetofrictional relaxation velocity and a radial outflow imposed at the source surface at 2.5 $R_\odot$, with characteristic width r_w and speed v_0. Imposing the former causes the magnetic field to tend towards a force-free equilibrium (Yang, Sturrock & Antiochos 1986), while the latter simulates the effect of the solar wind. Here, $v_0 = 100 \,\mathrm{km\,s^{-1}}$, $\nu = 60 \,\mathrm{km^2\,s^{-1}}$, and $r_w \approx 0.1 \, R_\odot$.

Resistivity is the only non-ideal effect, with the form

$$\vec{R} = \eta_c \vec{j} = \eta_0 \left(1 + \frac{1}{5}\frac{|\vec{j}|}{|\vec{B}|}\right), \tag{10}$$

where $\eta_0 = 60 \,\mathrm{km^2\,s^{-1}}$. This resistivity is enhanced in regions of strong current, and acts primarily to limit the amount of twist in strongly sheared magnetic fields.

2.2 Initial condition

The initial condition is constructed from an AFT map on 2014 September 1 at 12:00 UT. This map is taken as a lower boundary condition, from which a potential field source surface (Schmidt 1964) extrapolation is performed, out to a source surface at 2.5 $R_\odot$. The resulting three-dimensional magnetic field is used as the initial condition.

Since the coronal magnetic field is, in reality, highly non-potential, and the simulation begins from a potential field, the first 8 weeks of the simulation are taken to be a ramp-up period, during which time the simulation approaches a quasi-stationary, non-potential state. By 2014 November 1, such a state can be deemed achieved.

2.3 Inserting bipolar regions

Bipolar regions, representing newly emerged flux, are inserted according to the form prescribed by Mackay & van Ballegooijen (2006a), namely

$$B_x = B_0\sqrt{e}\left(\frac{z}{\rho_0}e^{-\xi} + 4\beta\frac{x'y'}{\rho_0^2}e^{-2\xi}\right) \tag{11a}$$

$$B_y = 2\beta B_0\sqrt{e}\left(1 - \frac{(x')^2 + z^2}{\rho_0^2}\right)e^{-2\xi} \tag{11b}$$

$$B_z = B_0\sqrt{e}\left(-\frac{x'}{\rho_0}e^{-\xi} + 4\beta\frac{y'z}{\rho_0^2}e^{-2\xi}\right), \tag{11c}$$

where (x', y') are local coordinates inside the bipolar region and z height above the photosphere; ρ_0 is the half-separation, namely half the distance between the peaks of the two opposing polarities; β a parameter regulating the self-twist of the bipolar region; ξ given by

$$\xi = \frac{\frac{1}{2}(x')^2 + (y')^2}{\rho_0^2}; \tag{12}$$

and B_0 a coefficient fixed by the total flux, Φ, in the bipolar region:

$$B_0 = \frac{\Phi}{\rho_0^2\sqrt{e\pi}}. \tag{13}$$

Both B_0 and Φ take the sign of the following polarity in the bipolar region. A bipolar region may be tilted at an angle γ_0, which is the angle between the meridian through the centre of the bipolar region and its local inversion line. In order to achieve tilt γ_0 in the bipolar region, the local coordinates (x', y') are rotated about the centre of the bipolar region (x_0, y_0):

$$x' = (x - x_0)\cos\gamma_0 - (y - y_0)\sin\gamma_0 \tag{14a}$$

$$y' = (x - x_0)\sin\gamma_0 + (y - y_0)\cos\gamma_0. \tag{14b}$$

Two regimes are considered for β. First, one case inserts all bipolar regions with $\beta = 0.0$, thereby inserting untwisted bipolar regions. Secondly, another case inserts bipolar regions with β of equal magnitude but opposing sign in the two hemispheres:

$$\beta = \begin{cases} -0.4 & \lambda > 0^\circ \\ +0.4 & \lambda < 0^\circ \end{cases}. \tag{15}$$

As can be seen from the helicity density associated with this form of bipolar region,[3]

$$\vec{A} \cdot \vec{B} = \beta \rho_0 B_0^2 e \left[2 - \frac{\left(x'\right)^2 + z^2}{\rho_0^2} \right] e^{-2\xi}, \tag{16}$$

the parameter β controls the self-helicity[4] with which each is inserted and, in particular, the sign of helicity. Accordingly, this latter choice of signs reflects a tendency for negative helicity to prevail in the Northern hemisphere, and positive in the southern, as has been observed (Pevtsov, Canfield & Metcalf 1994, 1995; Zirker et al. 1997). As demonstrated by Yeates et al. (2008, section 3.2 and table 2), this choice of magnitude for β most accurately reproduces the hemispheric distribution of the chirality of filaments observed (as by Rust 1967; Martin, Bilimoria & Tracadas 1994).[5] Comparing the two cases, $\beta = 0.0$ and $\beta = \mp 0.4$, is instructive in order to demonstrate how the formation and evolution of magnetic skew depend upon the presence of self-twist in new bipolar regions, along with the observed hemispheric preference in twist (as reported by Mackay & Gaizauskas 2003; Mackay & van Ballegooijen 2005).

While the form of bipolar regions inserted into the magnetofrictional simulations is highly idealized, this is sufficient, since the goal of these simulations is to study the global evolution of the coronal magnetic field as active regions decay and are transported poleward. As such, the decay of active regions and their interactions, with each other and with the ambient coronal field following their emergence, are most important. Such simulations are not intended, nor are they appropriate, to study the internal dynamics of active regions during their early emergence. However, to include the consequences of internal shear of newly emerged bipolar regions on the long-term coronal dynamics, some amount of skew associated with bipolar regions can be included through the parameter β. In particular, the angle of skew in a bipolar region of the form of equation (11) satisfies $\tan\gamma \propto -\beta$. When included, this skew is highest at the point of symmetry between the two polarities of the bipolar region and decreases with distance along the PIL towards the edge of the region.

2.4 Identification of bipolar regions and production of data set

In order to study the coronal magnetic field as accurately as possible, it is important that the photospheric field closely matches observations for the full duration of the simulation (2014 September 1 to 2015 March 30). Fundamental to this is the insertion of new bipolar regions as observationally detected, as done by Yeates et al. (2007).

Newly emerged bipolar regions are identified from the AFT simulations according to the process described by Mackay & Upton (2022, section 2.2.1). For each region detected, its properties – the signed flux, longitude, latitude, tilt, and half-separation between the two polarities – are determined.

Because new magnetic bipolar regions can only be observed from one vantage point at Earth, their properties can only be determined within a limited range of longitudes visible from Earth around central meridian. As such, this set of bipolar regions contains both those that emerge outside the Earth-bound field of view before subsequently rotating into it, and those that truly emerge within that field of view. All these bipolar regions are reported, and consequently only inserted into data-driven simulations, within that limited range of longitudes. However, this is not representative of the true evolution of the magnetic field on the Sun, where new flux may emerge at any longitude. How this affects our ability to model the production of strongly skewed fields at longitudes visible from Earth will be investigated in this work. In addition, three-fifths of the bipolar regions, and two-thirds of the total associated flux, emerge in the Southern hemisphere,[6] including the largest single bipolar region, which has flux $\Phi = 1.211 \times 10^{23}$ Mx and emerges on 2014 October 23.[7]

2.5 Analysis

For magnetic field lines passing over PILs, magnetic skew is understood in terms of the orientation of the magnetic field with respect to the underlying inversion line. First, the normal to the PIL is defined:

$$\hat{\vec{n}} = -\frac{\nabla_s \vec{B}_r}{\left|\nabla_s \vec{B}_r\right|}, \tag{17}$$

where ∇_s denotes the horizontal components of the gradient[8] and B_r the radial magnetic field component on the surface. Then, the angle of skew, γ, is defined as the angle between this normal and the horizontal magnetic field, $\vec{B}_h$, at some chosen height of interest (Martin & McAllister 1995, 1996):

$$\gamma = \sin^{-1} \frac{\left(\hat{\vec{n}} \times \vec{B}_h\right) \cdot \mathbf{e}_z}{\left|\vec{B}_h\right|}. \tag{18}$$

Here, that height is taken as being around 11 000 km. Where $\gamma > 0^\circ$, this corresponds to dextral skew, where $\gamma < 0^\circ$, this corresponds to sinistral skew. Throughout this work, the angle of skew is discussed in terms of its absolute value, $|\gamma|$.

Filaments typically exhibit an angle of approximately 20° (Leroy et al. 1983, 1984) between the filament's axis and its magnetic field. Since the filament's long axis follows the PIL, this corresponds to an angle of skew in the magnetic field of approximately 70°.[9] Skew in the simulations is understood to be 'strong' when exceeding this value, and 'weak' otherwise. Based on the angle of skew on each day, and how it varies from one day to the next, skew in the coronal magnetic field is divided into eight categories, listed in Table 1,

[3]Helicity density is here quoted using the vector potential for which the code solves, and as quoted in Yeates et al. (2007, equations 7–9). In general, a vector potential is not gauge-invariant, and therefore other forms of helicity density for the given field exist, in particular that relative to a potential field.

[4]Aside from self-helicity, there will also be mutual helicity, which may not be of the same sign.

[5]Dextral chirality corresponds to negative, and sinistral to positive, helicity (q.v. Mackay, Longbottom & Priest 1999).

[6]This is the consequence of a particular hemispheric asymmetry in solar cycle 24.

[7]that is, day 52 of the simulation.

[8]that is to say, the components tangential to the surface.

[9]Given an angle of 20° between the axis and the magnetic field, the complementary angle, between the normal to the axis and the magnetic field, is 70°.

Table 1. Categories into which points of skew in the magnetic field are divided. In plots showing skew by category, each category is represented by the colour specified in the second column. References to skew being 'above' or 'below' a given threshold are to be understood in terms of the absolute value. On any given day, skew is categorized according to its value on one day, and how that value compares with its value on the previous day.

Category of skew	Colour
Dextral, remaining below 70°	orange
Dextral, remaining above 70°	yellow
Dextral, currently above 70°, below 70° on previous day	red
Dextral, currently below 70°, above 70° on previous day	green
Sinistral, remaining below 70°	indigo
Sinistral, remaining above 70°	blue
Sinistral, currently above 70°, below 70° on previous day	purple
Sinistral, currently below 70°, above 70° on previous day	cyan

which quantify its evolution in time.[10] In later plots, each category is represented by the colour specified therein.

Given its association with filaments, the production of magnetic skew greater than 70° is the focus of this investigation. In order to identify where and when this strong skew appears, the change in the angle of skew on each day from the previous day must be determined. Skew is calculated above PILs, but these will evolve through translation and elongation. In order to compare the angle of skew at the same location between consecutive days, γ is interpolated from values along an inversion line on to a fixed longitude–latitude grid. Using this, the change in skew between consecutive days is easily calculated, allowing skew to be classified as in Table 1.

3 GLOBAL EVOLUTION

Fig. 1 compares the total flux, total magnetic energy, and total current in the two simulations studied, namely with $\beta = 0.0$ (represented by green lines) and with $\beta = \mp 0.4$ (represented by magenta lines).

Since both simulations start from the same initial state, and since each bipolar region inserted has the same flux irrespective of the self-twist (β) with which it is inserted, the total flux (solid; Fig. 1a) in the two simulations is the same (and hence one line overlies the other). During the first two days of the simulation, there is a rapid decrease in the total flux through the photosphere. This is the consequence of the AFT initial condition, which contains many small-scale polarities.[11] These small-scale polarities are quickly cancelled by the macroscopic diffusive processes, leaving only the large-scale long-lived flux patterns. After this early phase, the flux rises with the insertion of bipolar regions that are deduced from observations. Each bipolar region inserted causes a sharp increase, of varying size according to the amount of flux inserted. Largest is that on day 52, when a single bipolar region of 1.211×10^{23} Mx is inserted and accompanied by other smaller regions, as part of a larger complex of activity. At times when no bipolar regions emerge, the total flux reduces, through cancellation of oppositely signed flux.

Notably, a clear separation soon emerges between the open fluxes in the two cases (dashed lines in Fig. 1a). With $\beta = 0.0$ (green), the open flux is lower, and the difference grows over time. Open flux, in addition to that present in the initial state, is created through a range of non-potential processes (discussed by Mackay & Upton 2022, section 3.5), one of which is the eruption of flux ropes. With bipolar regions emerging twisted, flux ropes more readily form and erupt. As they do so, they carry their flux up to the top boundary, at 2.5 $R_\odot$. Upon reaching the boundary, the flux becomes open. Hence, the case with twisted bipolar regions ($\beta = \mp 0.4$; magenta) yields greater open flux as flux ropes form and erupt more frequently.

Magnetic energy is plotted as a function of time in Fig. 1(b). Starting from the same initial state, the total magnetic energy follows a similar trend in the cases with $\beta = 0.0$ (green) and with $\beta = \mp 0.4$ (magenta). In each, similar large sharp growths occur with each new bipolar region inserted. In the case with $\beta = 0.0$, however, the bursts are smaller and the total energy persistently lower than for $\beta = \mp 0.4$. This is a consequence of the untwisted bipolar regions ($\beta = 0.0$) being associated with lower energy. In general, the magnetic energy follows the evolution of the total flux.

Current evolves in a similar fashion (Fig. 1c). Initially, the potential field contains zero current, but surface motions and emergence of bipolar regions introduce coronal currents. Once again, sharp increases occur when the regions are inserted. Untwisted regions (with $\beta = 0.0$) carry less current, and so the growth in total current is smaller in that case (green) than in the case with $\beta = \mp 0.4$ (magenta). A fuller discussion of the global properties of the simulation can be found in Mackay & Upton (2022).

4 HOLISTIC VIEW OF SKEW

In order to analyse how strong skew forms and how long it persists, it is necessary to quantify the location and variation of skewed field lines over the duration of the simulation. In order to do so, the angle of skew of the magnetic field above PILs is calculated on each day of the simulation.

Figs 2 and 3 show a characteristic example, illustrating the results for 2014 December 10.[12] In each panel of Fig. 2, the properties of magnetic skew are shown above the underlying radial magnetic field on the solar photosphere. In those panels, white and black represent positive and negative flux, respectively. The scaling of the radial magnetic field is given by the first colour bar on the right-hand side. The entire path of PILs, which divide regions of positive and negative flux, is given by the coloured line in Fig. 2(a). In each plot, the vertical dashed red line denotes the longitude of the Sun lying at central meridian on the Sun–Earth line on that day. The vertical blue dashed lines show longitudes within 60° of central meridian, where the magnetic field can be measured accurately by existing magnetographs on the Sun–Earth line. From the distribution of the radial magnetic field, it can be seen that, at this stage in the solar cycle, the majority of the bipolar regions are concentrated near the equator. As a result of this, the paths of PILs are most complex between latitudes of ±40°, where there is a mixture of north–south and east–west orientations. Closer to the poles, the PILs appear smoother and more elongated. In each hemisphere, this is the result of the complexity in the radial magnetic field decreasing with latitude and differential rotation shearing and thus extending the PILs in an east–west sense. During the simulation, new PILs appear when new magnetic bipolar regions emerge. One part of the PIL separates the two polarities making up the bipolar region, and the

[10]These categories are disjoint but not exhaustive. For example, rare events, in which strong dextral skew on one day becomes weak sinistral skew on the next, would not fall in any category listed in the table.
[11]as shall be seen in Fig. 9(a).

[12]Animations of maps in Fig. 2 are available in online supplementary material.

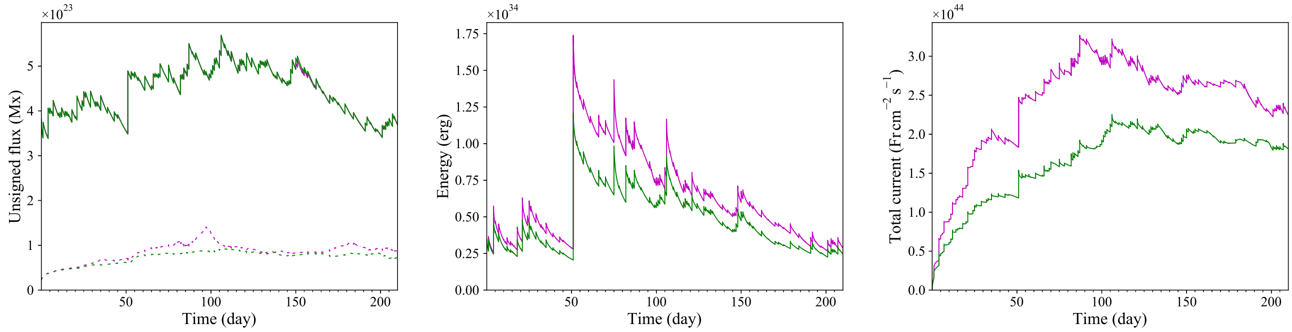

(a) Total and open flux. (b) Magnetic energy. (c) Total current.

Figure 1. Evolution over time of (a) surface and open magnetic flux, (b) total magnetic energy, and (c) total current. Shown here are simulations with bipolar regions inserted untwisted ($\beta = 0.0$; green) and with $\beta = \mp 0.4$ according to the sign of latitude, in order to match the observed hemispheric pattern in helicity (magenta). In (a), the total flux at the surface is shown by solid lines, the unsigned open flux by dashed. In (a), the solid green and magenta lines overlie each other, for the reasons discussed in Section 3.

other separates the bipolar region from the background field within which it emerges.

The coloured line in Fig. 2(a) represents the variation of the skew angle of the magnetic field along the entire path of PILs. Red and blue denote positive and negative γ, respectively, as indicated by the colour bar on the right-hand side. At locations where the angle skew is around 0° (green), the field lines lie nearly normal to the PIL and are close to potential. In contrast, for either chirality, where the angle of skew is around 90°, field lines lie parallel to the PIL and are highly non-potential. Strongly skewed field exists along most of the length of the PILs, both at low and at high latitudes, where, in each hemisphere, both dextral (red) and sinistral (blue) skew can be found. Strong skew often arises along the parts of PILs separating the opposite polarities making up bipolar regions. Examples of this can be seen at $(80^\circ, -20^\circ)$, $(160^\circ, -20^\circ)$, and $(260^\circ, -15^\circ)$, where sinistral skew is present, or at $(80^\circ, 5^\circ)$, $(160^\circ, 5^\circ)$, and $(290^\circ, 10^\circ)$, where dextral skew is present.

While Fig. 2(a) presents the overall skew on the 2014 December 10, Fig. 2(b) illustrates how the skew has changed along the PIL over the preceding 24 h. In this plot, red and blue denote, respectively, γ increasing and decreasing compared with the preceding day. Values for the change in skew are significantly less than those for the skew itself, and so the scale is restricted to the range $[-20^\circ, 20^\circ]$. From Fig. 2(b), it is clear that the change in skew is much more localized in nature, but can occur across all latitudes and longitudes.

In Fig. 2(c), magnetic skew is categorized according to Table 1, with the exception that the orange and indigo categories of weak skew remaining below 70° are omitted, which would otherwise obscure the remaining categories. Most prominent in this plot are the yellow and blue locations denoting, respectively, dextral and sinistral skew remaining above 70° from the previous day. These represent locations of strongly sheared fields, consistent with the angles measured within solar filaments, which persist above the PIL from one day to the next. Also prominent in this plot is the set of red regions around $(290^\circ, 10^\circ)$, which denote skew that has increased to be above 70° over the last 24 h and which are co-spatial with a region of increasing γ (red) in Fig. 2(b). Therefore, at these locations, skew has increased to become consistent with the orientation of the field measured in filaments and, as such, this set of locations represents where a filament channel has formed. Locations where the angle of skew has grown above 70° (red and purple) are significantly fewer in number and smaller in area than those where strong skew persists (yellow and blue).

While Fig. 2 illustrates PILs according to the angle of skew along them, Fig. 3 shows field lines in the corona. These are shown in two-dimensional projections (a) and in three dimensions (b), in which the central meridian of the Sun is chosen to match that observed on 2014 December 10. In each, the underlying photospheric magnetic field is shown as in Fig. 2. In Fig. 3(a), examples can be seen of both dextral- and sinistral-skewed field lines, where the angle of skew along these field lines is shown by Fig. 2(a). Around the bipolar region at $(255^\circ, -15^\circ)$, field lines starting in the area of positive polarity (white) clearly veer leftwards as they cross the underlying inversion line towards the negative polarity (black). This sinistral skew (blue) can be seen at the corresponding location in Fig. 2(a). Dextral skew is illustrated by the bipolar region at $(290^\circ, 10^\circ)$, where field lines cross the inversion line, from positive polarity (white) to negative (black), inclined to the right. Positive γ (red–orange) at the same location in Fig. 2(a) indicates this chirality.

To quantify the overall properties of the skew over the entire duration of the simulation and over the full Sun, Fig. 4 plots several integrated quantities: (a), (d) the length of PILs with dextral or sinistral skew; (b), (e) the average angle of dextral or sinistral skew over all PILs; and (c), (f) the proportion of the length of PILs with strong dextral or sinistral skew. In each panel, dextral skew is denoted by a red curve and sinistral skew by blue, while black gives the results for total (dextral and sinistral) skew. The top row shows results for the case where $\beta = 0$ and the bottom row for $\beta = \mp 0.4$.

Over the first ten days of the simulation, there is a rapid decrease in the length of PILs along which there is dextral (red) or sinistral (blue) skew (Figs 4a and d). After this rapid decrease, each settles to a relatively constant value for the remainder of the 210-d duration of the simulation. The reason for the rapid decay in the total length of PILs with dextral or sinistral skew is that the magnetogram used as the initial condition contains a large number of small magnetic elements. These produce a fine-scale structuring of PILs, close to the resolution of the numerical grid. However, surface diffusion quickly removes this fine-scale structuring, producing the smooth large-scale paths shown in Fig. 2(a). While the lengths of PILs with dextral and sinistral skew differ between the two simulations, the total length of PILs (black) is the same for both simulations at any one time. For most of the duration of the simulations, it is around 3.2×10^{10} m (Figs 4a and d).

While the total length of PILs is the same, the strength of skew along them varies between the cases with $\beta = 0.0$ and $\beta = \mp 0.4$. Initially, the average skew decreases with time (Figs 4b and e) in

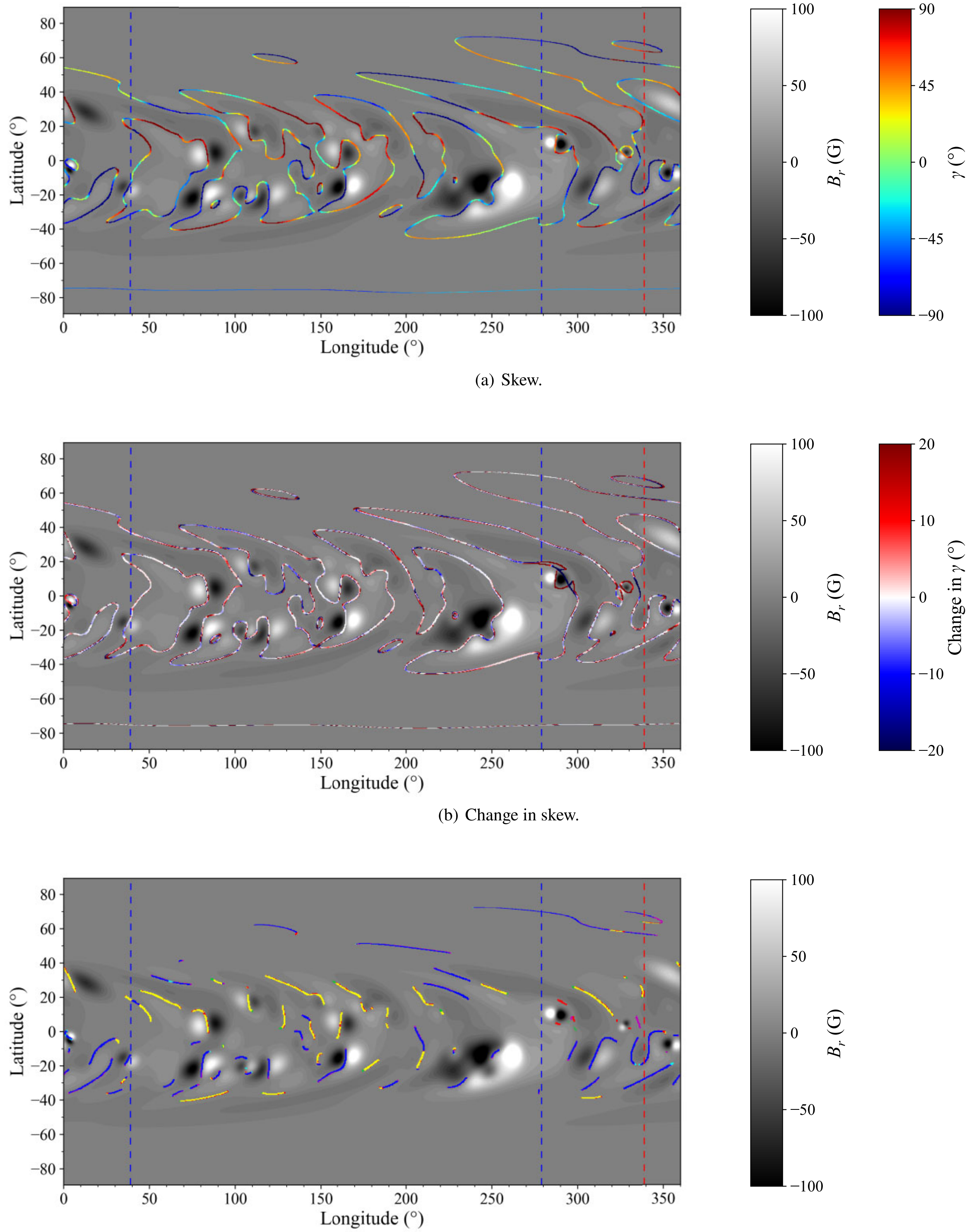

(a) Skew.

(b) Change in skew.

(c) Category.

Figure 2. Maps of the radial photospheric magnetic field, where white and black represent positive and negative polarity, respectively. Superimposed on top of those, in the first three panels, are areas of skew above PILs shaded (b) according to the angle γ; (b) according to the difference in γ between the current day and the previous; and (c) according to the categories of Table 1, each in the corresponding colour given therein. Each of B_r, γ, and the change in γ is represented according to the relevant colour bar shown. In (a), (b), and (c), the dashed red vertical line represents central meridian, and the dashed blue lines the bounds of the field of view. In order to demonstrate the location and identification of skew, the coronal field on 2014 December 10 is represented. On this day, the central meridian is at 339°. Here, the case with bipolar regions inserted having $\beta = \mp 0.4$, according to the sign of latitude, in order to match the observed preference in helicity, is presented. Animations of these maps are available in online supplementary material.

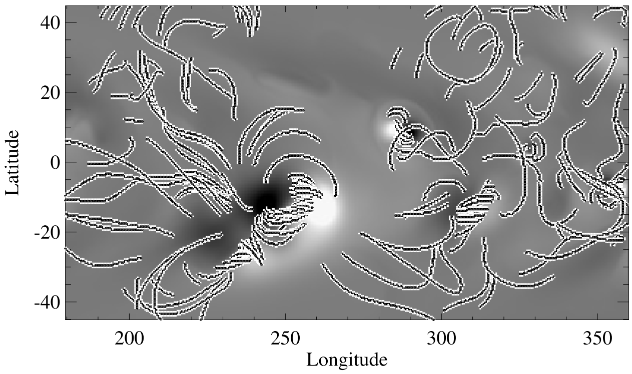

(a) Field lines in two dimensions.

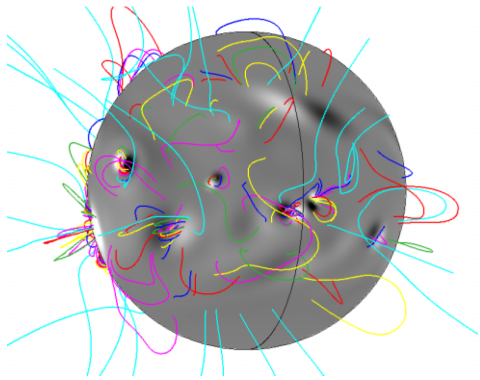

(b) Field lines in three dimensions.

Figure 3. Maps of the radial photospheric magnetic field, where white and black represent positive and negative polarity, respectively. In each plot, the same illustrative set of field lines is superimposed upon similar two- and three-dimensional maps of the photospheric magnetic field. In (a), a 180°-wide view is plotted, aiming to represent the field of view and the portion of the Sun visible in (b), but, in order to avoid wrapping around 0°, the range shown is [0°, 180°]. In (b), the view seen is centred on central meridian. In order to demonstrate the location and identification of skew, the coronal field on 2014 December 10 is represented. On this day, the central meridian is at 339°. Here, the case with bipolar regions inserted having $\beta = \mp 0.4$, according to the sign of latitude, in order to match the observed preference in helicity, is presented.

both simulations. This occurs as the small-scale structure in the initial condition is removed. This decrease represents the fact that the initial small-scale structure in B_r, which creates coarse photospheric PILs, does not extend to a significant coronal height. In the corona, the field is smoother, giving the false impression of strong skew of the coronal field relative to the underlying photospheric PIL. After the first few days, this small-scale structure is removed and, in each simulation, the unsigned average skew increases until around day 50 as a consequence of flux transport effects. This represents the transition from the initial potential field to a non-potential configuration. After that, a nearly steady state is found for each of dextral and sinistral skew. Such a steady state indicates the approximately equal formation and ejection of skew. Between days 10 and 50, the total length of PILs remains nearly constant. Therefore, the increasing levels of skew are caused by the growth of skew along existing PILs, rather than by the appearance of new PILs with strongly skewed fields. On comparing the two simulations, it can be seen that, when bipolar regions emerge twisted, slightly higher values of the average skew are found. In particular, the mean skew increases from around 55° ($\beta = 0.0$; Fig. 4b) to around 60° when twist in the bipolar regions is included ($\beta = \mp 0.4$; Fig. 4e). Over the final fifty days of the simulation, the average angle of skew reaches nearly 60° for the case without twist ($\beta = 0.0$) and 65° for the case with twist ($\beta = \mp 0.4$). During the period studied, most bipolar regions emerge south of the equator, where skew is typically sinistral. As a result, where bipolar regions emerge twisted, there is a greater increase in sinistral skew than in dextral (Fig. 4e). This can be seen in Figs 4(b) and (e), where for the case with $\beta = 0.0$, levels of dextral and sinistral skew are consistently similar, but the case with $\beta = \mp 0.4$ shows sinistral skew almost always greater than dextral (Fig. 4e).

Finally, in Figs 4(c) and (f), the fraction of the length of the PILs with dextral or sinistral skew above 70° is presented. This quantifies the length of the PILs exhibiting a strongly sheared field, as is consistent with that found within a filament channel or filament. Following the behaviour found in Figs 4(b) and (e), the length of PILs with strong skew rapidly increases between days 10 and 50, after which a nearly steady level is found. For the same reason that the mean angle of skew increases during that interval, strong skew also prevails along a greater fraction of the total length of PILs. In the simulation with $\beta = 0$, only between 30 per cent and 40 per cent of the length of PILs generally exhibits strong skew (Fig. 4c), whereas this increases to between 35 per cent and 45 per cent of PILs in the simulation in which $\beta = \mp 0.4$ (Fig. 4f).

Overall, when the skew in both simulations is compared in terms of these integrated quantities, very few differences arise between the two simulations. Any that do are relatively minor. The most notable difference is that the simulation including twisted bipolar regions ($\beta = \mp 0.4$) produces a more strongly skewed magnetic field than does the untwisted case ($\beta = 0.0$).[13] The fact that this difference is small indicates that bipolar regions that emerge with twist are not the main source of shear in the simulation over long periods of time.

4.1 Area of skew over the whole Sun

While it is useful to consider the angle of skew instantaneously along PILs, an alternative approach is to interpolate γ from PILs on to the model's fixed grid (as discussed in Section 2.5). Doing so allows the change in skew from one day to the next to be determined. Fig. 5 plots against time the areas of the Sun where skew is classified in terms of each of the several categories defined in Table 1 (each represented by a curve of the colour given in the table). In the two simulations, with $\beta = 0.0$ and with $\beta = \mp 0.4$, these areas evolve similarly.

Initially, skew below 70° exists over large areas (orange and indigo curves in Figs 5a and b), as a consequence of the small-scale variations in the initial condition (as discussed in Section 3). As these small-scale variations are removed, these areas of skew fall, and this contributes to a reduction in the areas represented by the orange and purple curves. By around day 50, they reach a steady level.

While the cancellation of small-scale PILs is one contributor to the decrease in the area where there is weak skew, another is the growth of the angle of skew above 70°. As the angle of skew at individual points crosses the threshold $|\gamma| = 70°$, the area associated with those points transfers from the orange and indigo categories to the yellow and blue categories, respectively. Over the first 50 days, in both simulations, the area of strong skew rises steadily, but slightly faster in the case with $\beta = \mp 0.4$ (Figs 5a and b). After the first two months, the areas where there is strong skew are nearly steady. For the case of bipolar regions being inserted with $\beta = \mp 0.4$, strong dextral

[13] For both untwisted and twisted bipolar regions, it should be noted that the photospheric distribution and thus the total length of the PILs are the same.

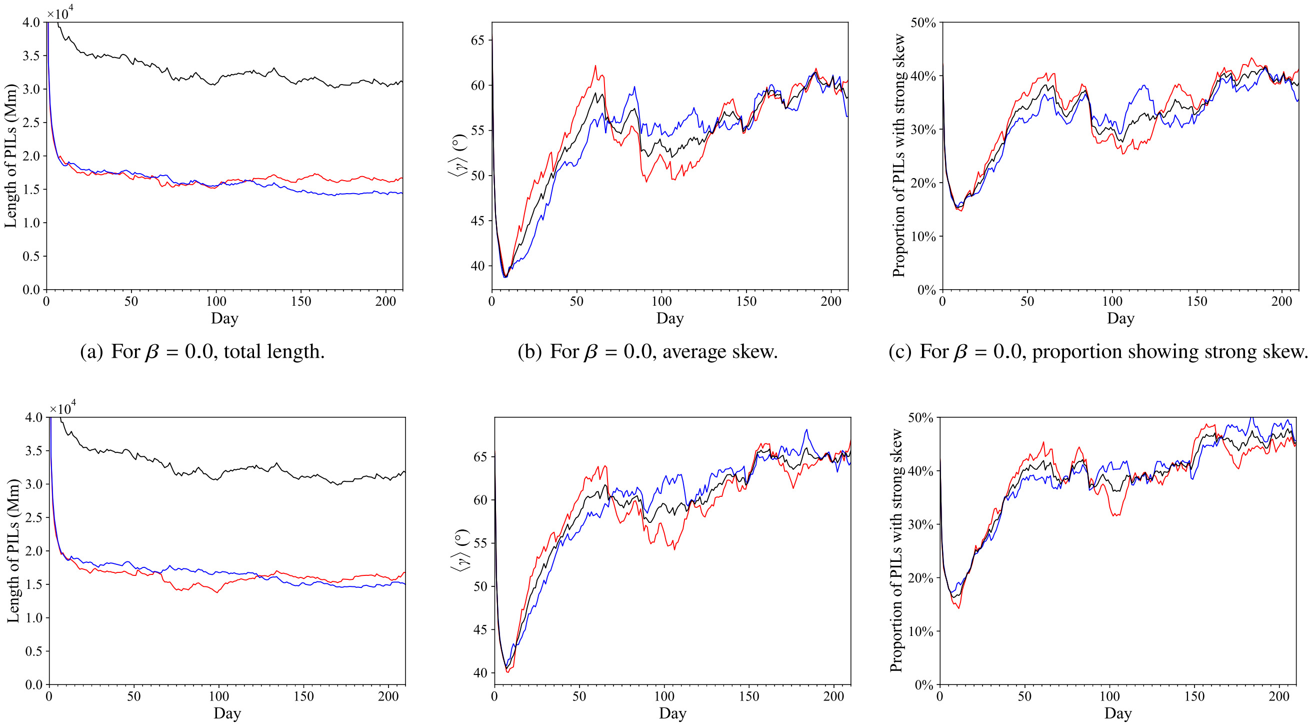

(a) For β = 0.0, total length. (b) For β = 0.0, average skew. (c) For β = 0.0, proportion showing strong skew.

(d) For $\beta = \mp 0.4$, total length. (e) For $\beta = \mp 0.4$, average skew. (f) For $\beta = \mp 0.4$, proportion showing strong skew.

Figure 4. Along PILs, (a), (d) their total length of PILs, (b), (e) the average angle of skew, and (c), (f) the fraction of their total length where the field is strongly skewed ($|\gamma| > 70^\circ$). Dextral, sinistral, and total skew are shown in red, blue, and black, respectively. Results are compared for simulations inserting bipolar regions with (a), (b), (c) no self-twist ($\beta = 0.0$) and (d), (e), (f) self-twist matching the hemispheric pattern in helicity ($\beta = \mp 0.4$).

and sinistral skew each prevail over an area around 7×10^{16} m^2 (Fig. 5b). However, with untwisted bipolar regions, strong skew is seldom present over quite so large an area, generally around 5–6 $\times$ 10^{16} m^2 ($\beta = 0.0$; Fig. 5a). This indicates that bipolar regions that emerge with twist are more likely to create stronger skew as they subsequently evolve and interact with the coronal magnetic field.

Despite the fact that the areas with skew remaining above 70° are relatively steady, the areas where the angle of skew grows above 70° (red and purple) consistently appear to outweigh the areas where it falls below 70° (green and cyan). For each chirality, the area where the angle of skew grows above 70° is around 1×10^{16} m^2, and the area where it falls below 70° around 3×10^{15} m^2. At first, this difference between these areas of growing and diminishing skew seems counter-intuitive. However, there are two reasons that the difference between these areas does not equal the rate of change of the area where skew is above 70°.

First, the areas where the magnetic field is skewed can change in two ways. As PILs grow in length and as flux ropes form and grow, the area where there is strong skew slowly and continually increases. On the other hand, aside from the angle of skew decreasing, strong skew can also be removed rapidly through the eruption of flux ropes, which decreases the total area where there is strong skew. Following such an eruption, the underlying PIL, relative to which skew is calculated, remains. However, the highly skewed flux rope above it has been removed. In its place, the angle of skew is around zero.[14] When the slower growth of skew balances its local rapid elimination through ejection, the areas of persistent strong skew (yellow and blue) are steady.

Secondly, differential rotation has a tendency to cause existing areas where there is strong skew to expand. It is far less likely to cause them to reduce. Fig. 6 illustrates this difference by considering the way in which it acts on flux ropes (brown). Fig. 6(a) shows the typical situation on the Sun. Parts of flux ropes closer to the equator (which is shown in black) will be carried eastwards by differential rotation (represented by green arrows) faster than parts further away from the equator. Consequently, north–south flux ropes will be sheared and thereby elongated, thus increasing their area. Seldom will differential rotation reduce flux ropes in length: only flux ropes running from south-west to north-east in the Northern hemisphere, and from north-west to south-east in the southern, are affected in this way (similarly illustrated in Fig. 6b). Differential rotation thus creates a way in which the area where there is strong skew can expand, and the total area of strong skew thus increases, aside from the angle of skew growing from below 70° to above 70°, as would fall in the category of strengthening skew.

4.2 Area of skew within the Earth-bound field of view

While quantifying the presence of magnetic skew over the entire Sun is useful, this does not reflect what would be observed from Earth. For that reason, it is instructive to quantify over time the changes in skew that would be seen within the Earth-bound field of view, namely within 60° of central meridian, as the Sun rotates.

Fig. 7 plots against time the area within the Earth-bound field of view where there is skew of each category given in Table 1. In order

[14] As such, the skew at the location where the flux rope lay may not be categorized as dextral or sinistral skew above 70° falling to be skew of the same sign below 70°, and thus that location not counted in the two categories of falling skew in Table 1.

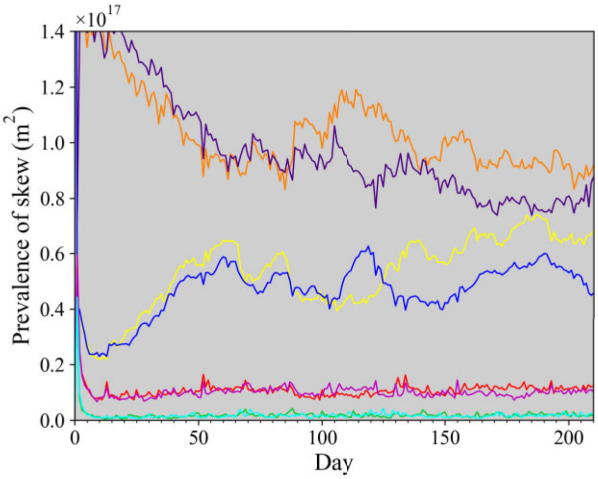

(a) For $\beta = 0.0$, across the whole Sun.

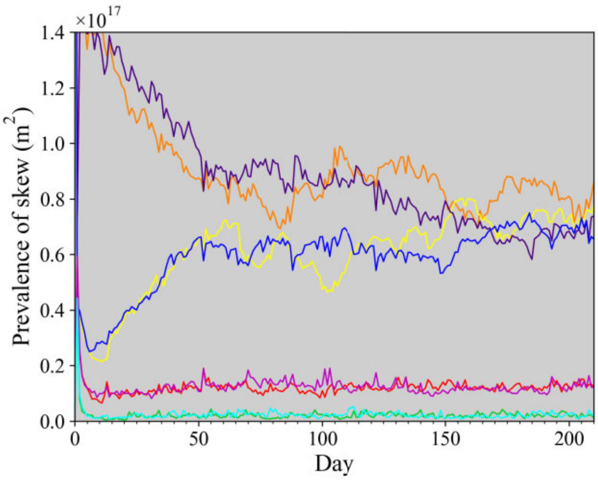

(b) For $\beta = \mp 0.4$, across the whole Sun.

Figure 5. Plotted against time, the areas above which skew falls within the several categories of Section 2.5 and Table 1, each represented by a curve in the corresponding colour, across the whole surface of the Sun. Results are compared for simulations inserting bipolar regions (a) with no self-twist ($\beta = 0.0$) and (b) with self-twist matching the hemispheric pattern in helicity ($\beta = \mp 0.4$).

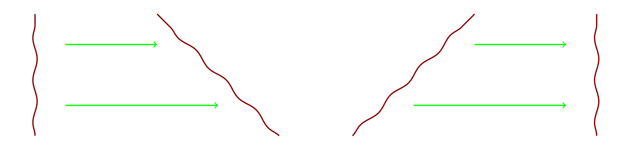

(a) Filament lengthening. (b) Filament shortening.

Figure 6. Effect of differential rotation on filaments. Differential rotation imposes velocities (green arrows, longer for faster velocities) that act upon a filament (brown) as seen on the left of each panel, shear it, morphing it into the shape shown on the right. Here, the effect on filaments in the Northern hemisphere is illustrated; in the Southern hemisphere, a similar effect would be seen, mirrored in the equator (black). Depending on the initial configuration of the filament, the effect of differential rotation may (a) elongate or (b) shorten the filament.

that the graphs are more easily readable, it is useful to separate, on one hand, areas where skew remains above or below 70° and, on the other, areas where skew grows above or falls below 70°. For that reason, they are shown on different scales, the former in (a) ($\beta = 0.0$) and (b) ($\beta = \mp 0.4$), and the latter in (c) ($\beta = 0.0$) and (d) ($\beta = \mp 0.4$). In these results, some facts are quite prominent. Large undulations appear in the areas of skew remaining below 70° (orange and indigo) or above 70° (yellow and blue), which recur approximately every twenty-seven days .[15]

As a demonstration of this, Fig. 8(a) shows a Fourier transform of the area of strong dextral skew ($\gamma > 70°$) in the field of view as a function of time, from the case with $\beta = \mp 0.4$ (namely, the yellow curve in Fig. 7b). Power present in oscillations of a given period is plotted against that period. For periods longer than around 70 d, there are too few data points, and thus the Fourier transform becomes unreliable at those periods. Strikingly, the Fourier transform peaks at a period of 26.375 d (dashed red vertical line), this being the data point closest to the Carrington rotation of 27.2753 d (Stenflo 1990).[16] For a given location of strong skew in the field of view, this period is the mean time for that location to leave the field of view, to pass over the far side of the Sun, and to re-enter the field of view. Given the concentration of power at this period, much of the variation in the area of strong skew is provided by the periodic return of relatively steady magnetic configurations to the Earth-bound field of view.

In order to illustrate such a periodic return occurring, it is worthwhile to consider the specific example of a bipolar region which emerges at (121°, 9°) on December 23 (day 113) and which produces a feature of strong dextral skew. To do so, Fig. 8(b) plots the total area of weak (orange) and strong (yellow) dextral skew against time. Highlighted in green are the times when this magnetic bipolar region lies within the field of view observable from Earth. This bipolar region first enters the field of view on day 112, but, at this time, there is no enhancement of the strong skew compared with that found approximately twenty-seven days earlier. This is because the area associated with the bipolar region is small, and so, on its first rotation through the field of view (days 112 to 121), it makes only a small contribution to the total skew above 70°. As the bipolar region evolves on the far side of the Sun, its magnetic field slowly evolves and an area of strong skew develops around it. When this magnetic configuration next enters the field of view (day 139), the area of strong dextral skew has a much higher peak, but, when this configuration leaves (day 148), this area declines. This process occurs two further times (between days 166 and 175, and between days 193 and 202), as the bipolar region successively returns to the field of view observable from Earth. In the total area of weak dextral skew (orange), there is a periodic effect similar to that in the total area of strong dextral skew. That additional effect is the result of the presence of other features of weak dextral skew leaving and re-entering the Earth-bound field of view, alongside the feature of strong skew discussed. In the two earlier highlighted intervals (days 112 to 121, and 139 to 148), the peaks in the total area of weak dextral skew occur slightly earlier than do those in strong dextral skew, in part because, as the flux rope associated with the bipolar region grows, locations of weak skew become locations of strong skew.

[15] In particular, this is strongly apparent here in the orange and yellow curves.
[16] Since this period is an average, rotation of features spanning several latitudes will contribute to a periodic effect across a range of time-scales from 26 to 38 d. In part, the limited fineness of the discretization in time masks this, with many periods subsumed into the one point.

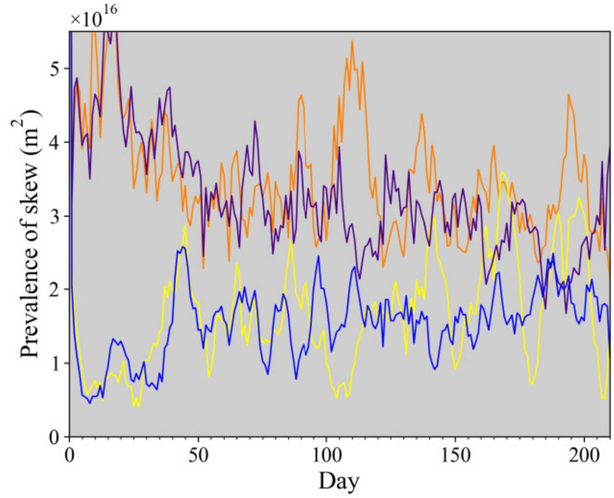

(a) For $\beta = 0.0$, skew in view remaining above or below 70°.

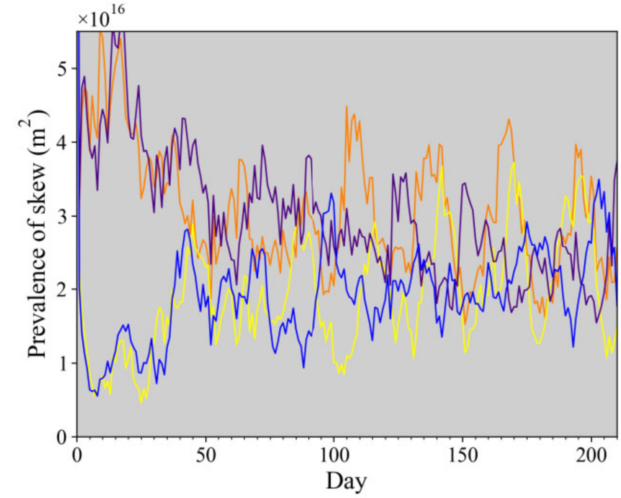

(b) For $\beta = \mp 0.4$, skew in view remaining above or below 70°.

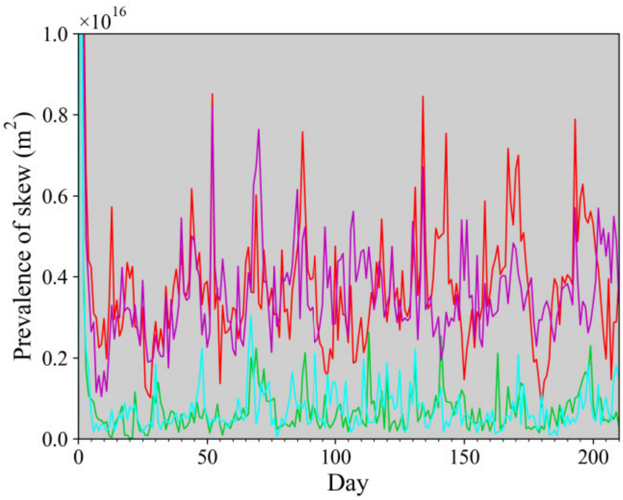

(c) For $\beta = 0.0$, skew in view crossing 70°.

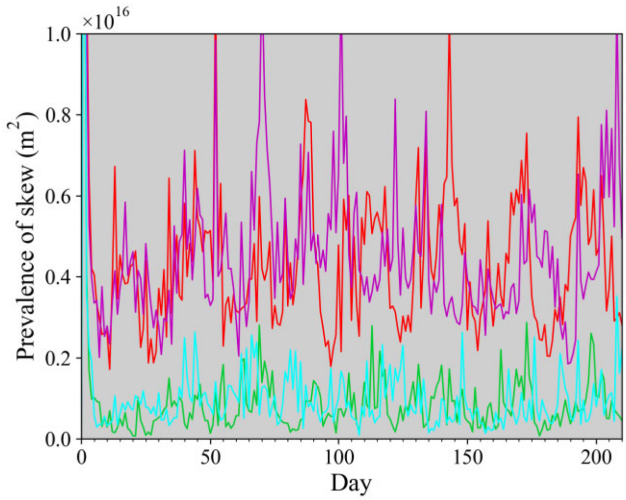

(d) For $\beta = \mp 0.4$, skew in view crossing 70°.

Figure 7. Plotted against time, the areas above which skew falls within the several categories of Section 2.5 and Table 1, each represented by a curve in the corresponding colour, within the field of view. Results are compared for simulations inserting bipolar regions (a), (c) with no self-twist ($\beta = 0.0$) and (b), (d) with self-twist matching the hemispheric pattern in helicity ($\beta = \mp 0.4$). Between (a), (b), and (c), (d) are split areas of skew remaining above or below 70° and skew crossing that threshold, in either direction, on account of the different scales spanned and in order that the latter smaller categories not be obscured.

While the large periodic behaviours seen in Figs 7(a) and (b) correspond to large features of strong skew entering and leaving the field of view, the total areas where skew grows above 70° or falls below 70° show a different evolution: no such periodic variations appear (Figs 7c and d). Areas of skew in these categories are identified by a change in the angle of skew from one day to the next. As such, these categories specifically select locations where magnetic skew evolves in a particular way, and thus exclude structures where skew is relatively steady and which merely translate through the coordinate system. Such relatively steady magnetic structures, as they enter and leave the Earth-bound field of view, create the strong oscillations seen in Figs 7(a) and (b). Thus, by excluding these structures, the categories of growing or reducing skew (Figs 7c and d) are far less affected by periodic variations.

Aside from such periodic variations, the analysis of the total areas of skew of different categories raises two important questions. The first is how likely it is that skew of each category lies in the Earth-bound field of view. The second is how likely it is that the skew of each category found within the field of view forms there.

Regarding the first question, it is clear that the total area of weak skew of either chirality (orange or indigo), in either simulation, is generally around 10^{17} m^2 over the whole Sun. Within the Earth-bound field of view in either simulation, it is around 3×10^{16} m^2. Similarly, the simulated area of strong skew of either chirality over the whole Sun is around $5–7 \times 10^{16}$ m^2, of which around $1.5–2 \times 10^{15}$ m^2 lies within the field of view. Evidently, skewed magnetic structures are dispersed across all longitudes on the Sun, and, as one-third of the Sun is visible from Earth, so around one-third of these structures are within the field of view. However, this does not indicate where strong skew has formed, nor how likely it is to form within this field of view.

Regarding the second question, the areas where skew within the field of view grows to be strong (red or magenta), or falls to be below 70° (green or cyan), represent areas where new strong skew is created or where existing strong skew is removed within the field

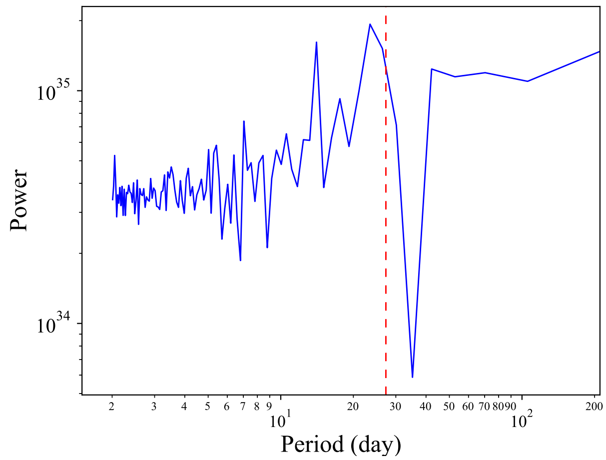

(a) Fourier transform of area of strong skew win field of view.

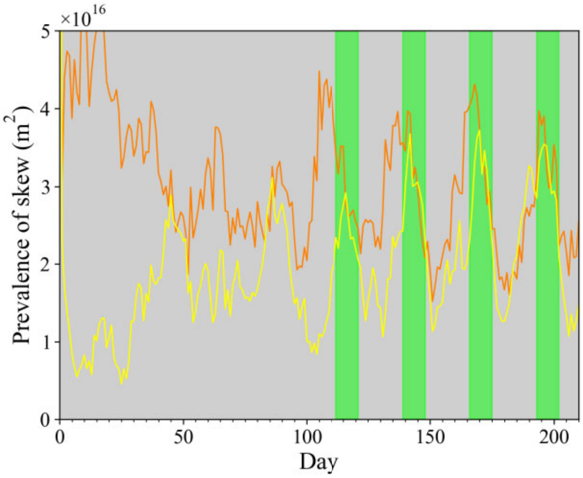

(b) Highlighting when a particular feature is in the field of view.

Figure 8. Oscillations in area of strong dextral skew in field of view (that is, the yellow curve in Fig. 7b), as individual features rotate into and out of view. (a) Fourier transform, plotted against period, of the area within the field of view above which there is dextral skew greater than 70°. As a result of limited cadence for output of the data, the peak occurs at 26.375 d (indicated by a dashed red vertical line), the closest point to the Carrington rotation period, 27.2753 d. As the simulations span only 210 d, there are three or fewer data points for periods of 70 d or longer, and so the transform becomes unreliable. (b) Total area of weak (orange) and strong (yellow) dextral skew within the field of view, highlighting in green the periods when a feature originating at (121°, 9°) lies within the field of view. As this large feature periodically returns to the field of view, the total area is significantly enhanced. Each green band is offset 27 d from the previous one, corresponding to the period of solar rotation, and is 9 d wide, corresponding to the interval between one location entering and leave the field of view.

of view. Clearly, the areas associated with these locations, which are being added to the total areas of strong or weak skew on any one day, seldom exceed 6×10^{15} m^2 (Figs 7c and d). However, the periodic oscillations in Figs 7(a) and (b), which indicate strong skew entering and leaving the field of view, have amplitudes typically of the order of at least 10^{16} m^2. Therefore, most of the strong skew in the field of view, shown in Figs 7(a) and (b), exists in the field of view as a result of the rotation of pre-existing strong skew into the field of view, rather than as a consequence of the production or growth of new strong skew within it. This is a strong indicator of a fundamental property, namely the long-term persistence of skew, which typically lasts longer than the time-scale for solar rotation.

How far growing skew outweighs diminishing skew varies significantly with the presence ($\beta = \mp 0.4$) or absence ($\beta = 0.0$) of self-twist in bipolar regions. In both cases, the areas of dextral and sinistral skew falling below 70° fluctuate around 1×10^{15} m^2, whereas the areas of growing skew fluctuate around 3×10^{15} m^2 for $\beta = 0.0$ (Fig. 7c) and 4×10^{15} m^2 for $\beta = \mp 0.4$ (Fig. 7d). Consistently, inserting twisted flux leads to the more rapid creation, and to the greater total creation, of strong skew.

5 LOCAL EVOLUTION OF SKEW

Using area-integrated quantities, as in Section 4, the prevalence of skew over the entire Sun can be easily considered. However, for studying the formation of filaments, it is important to consider specific locations at which there are large contiguous regions of strong skew ($|\gamma| > 70°$). Here, the appearance and evolution of such regions are discussed for the case where $\beta = \mp 0.4$, because this is a more realistic representation of non-potential bipolar regions on the Sun, which has been shown to produce the known hemispheric pattern in chirality (Yeates et al. 2007).

Fig. 9 shows maps of the photospheric magnetic field (B_r) over several different days, in the same format as Fig. 2(c). On top of these maps, areas with skew in each category are shaded in the colour given in Table 1. Locations where skew remains below 70° (orange or indigo) are not shaded, as they would otherwise obscure the image. Locations of interest, where strong skew lies or is produced, are circled in brown. As time progresses, the central meridian (dashed red) and the bounds of the field of view (dashed blue) move towards decreasing longitudes at a rate of 13.2° per day.

At the start of the simulation (2014 September 1; Fig. 9a), the calculated magnetic skew is dominated by the nature of the initial condition. Within the initial condition, numerous small patches of mixed positive (white) and negative (black) polarity create significant small-scale variation along PILs. Those small-scale variations produce random structuring of PILs, which is associated with non-zero skew (as discussed in Section 4). Only a small amount of this skew exceeds 70° (yellow or blue), occurring only in small fragments. Within a few days (e.g. September 13; Fig. 9b), these small-scale regions have mostly vanished, after the combined actions of SFT and surface diffusion have removed them. Following this, the magnetic field is smoother and shows variations on a larger scale.

After this early evolution, small instances of the formation of skew above 70° within the Earth-bound field of view occur. For example, dextral skew grows at a location around (20°, −45°), beginning on September 13 (seen in red in Fig. 9b). After this location has left the same field of view, by September 23 (at $\lambda = -45°$ in Fig. 9c), the magnetic feature of strong dextral skew (yellow) is much larger, and extends between longitudes 350° and 10°.

Such instances of the initial formation of strong skew within the field of view from Earth are comparatively rare. With observations available only on the Earth-facing side of the Sun, larger regions of strong skew at longitudes visible from Earth are more likely to form outside and to be carried by solar rotation into the Earth-bound field of view, rather than to form therein, in line with the results of Section 4.2. During the remainder of the month, prominent examples of the rotation of strong skew into the Earth-bound field of view include strong dextral skew (yellow) at (150°, 15°) and at (150°, 70°) on September 30 (Fig. 9d). Both of these are areas of persistent skew that have appeared over the limb and rotated into longitudes visible from Earth (demarcated by vertical dashed blue) as a consequence

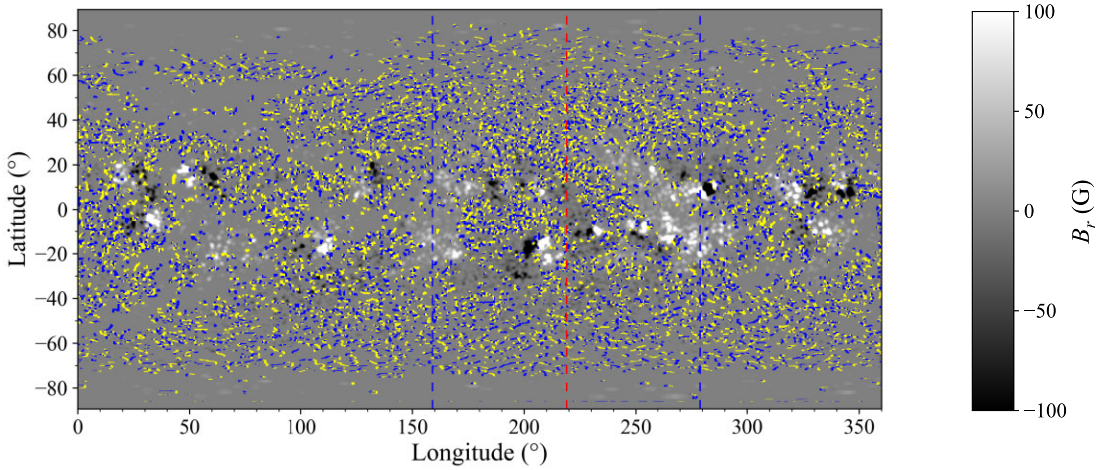

(a) Initial state (1 September).

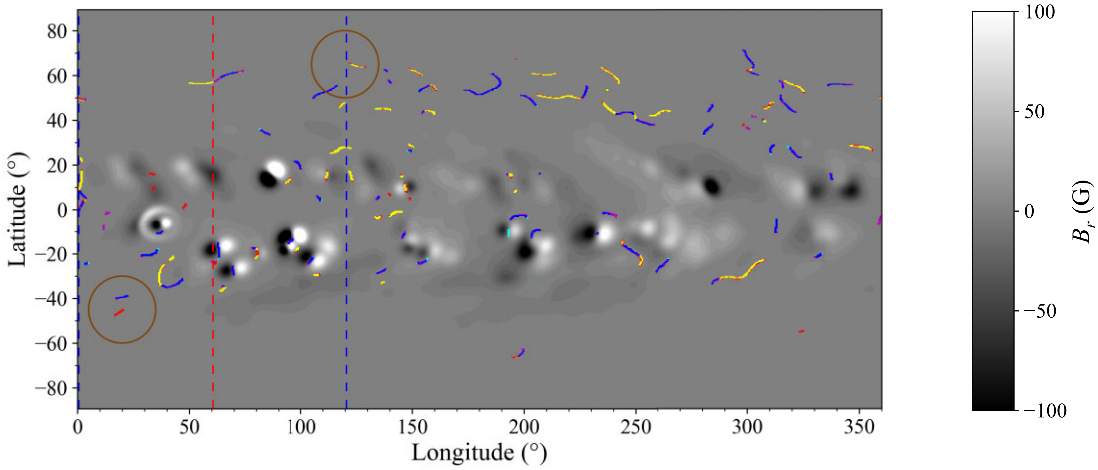

(b) 13 September.

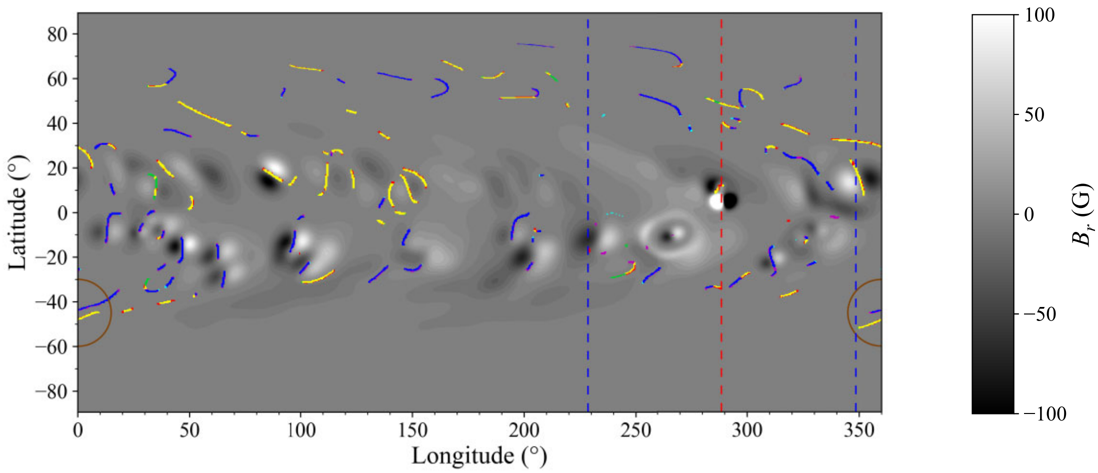

(c) 23 September.

Figure 9. In the format of Fig. 2, maps of the radial photospheric magnetic field, according to the colour bar shown, with, superimposed on top of those, areas of skew above PILs, shaded according to Table 1. As in Fig. 2, the vertical dashed blue lines represent the bounds of the field of view, dashed red central meridian; sections of PILs where skew remains below 70° are omitted; and the case with bipolar regions inserted with $\beta = \mp 0.4$ is presented.

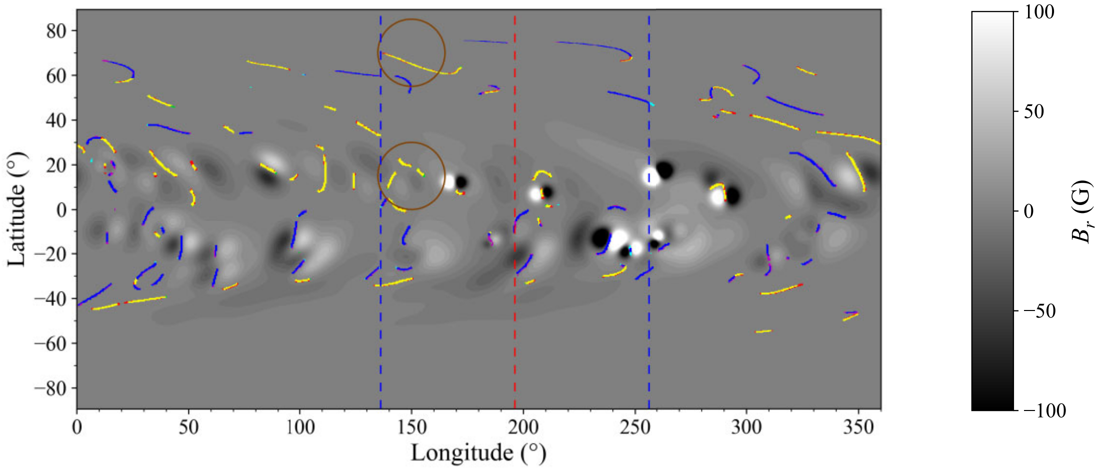

(d) 30 September.

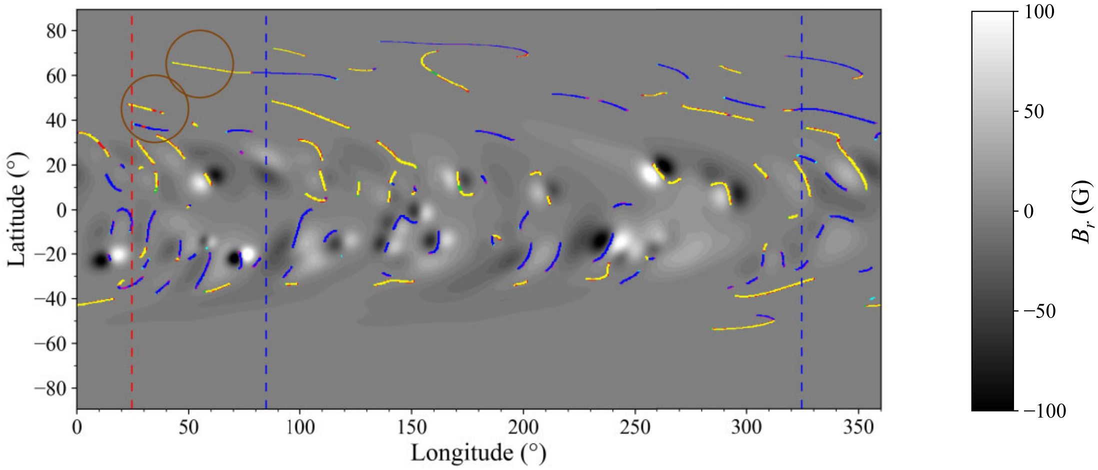

(e) 13 October.

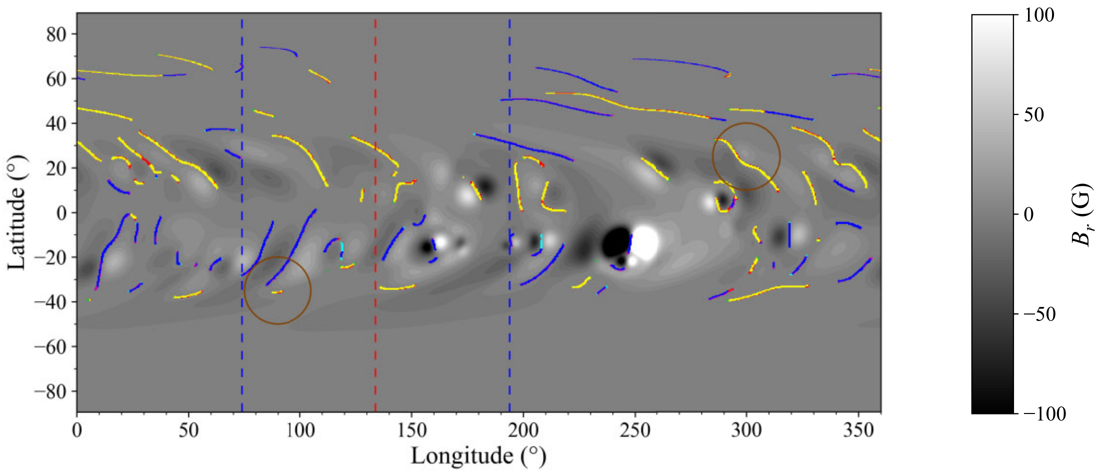

(f) 1 November.

Figure 9. – *continued*

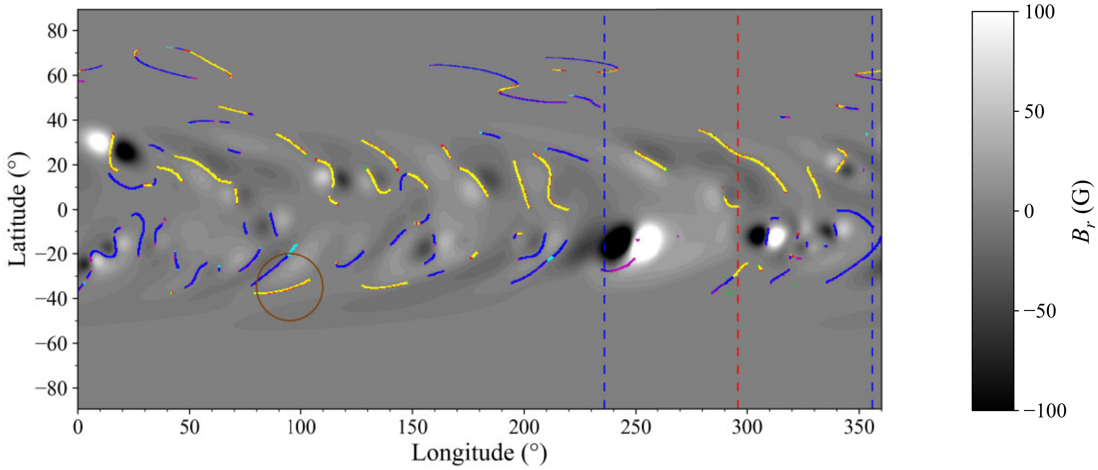

(g) 16 November.

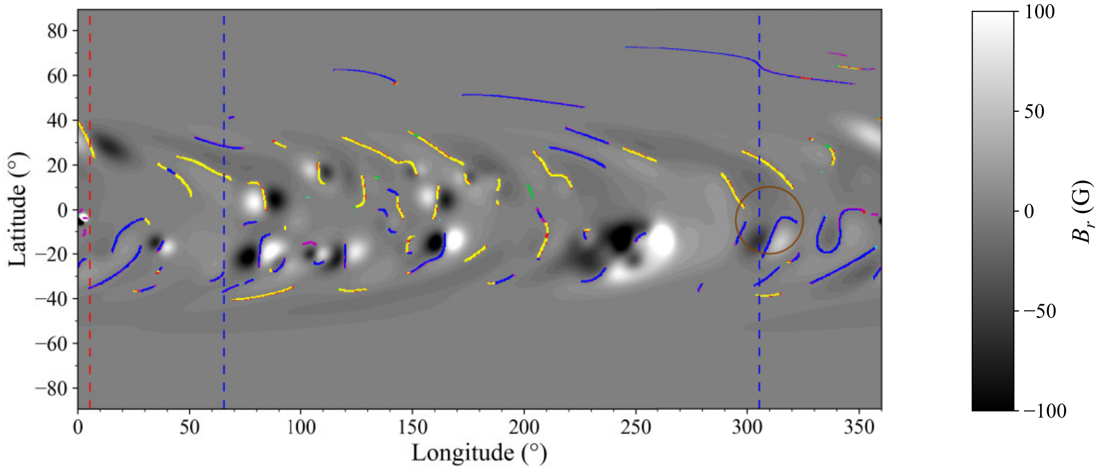

(h) 8 December.

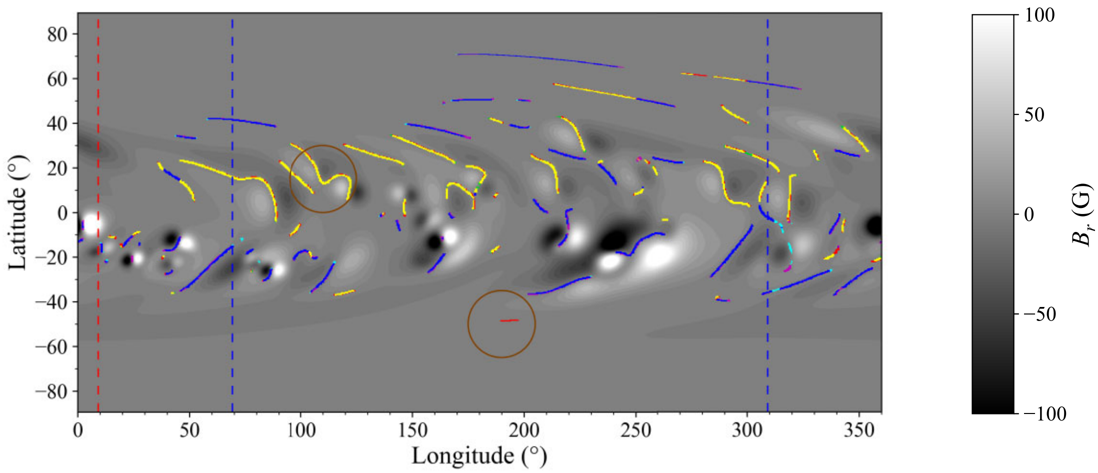

(i) 4 January.

Figure 9. – *continued*

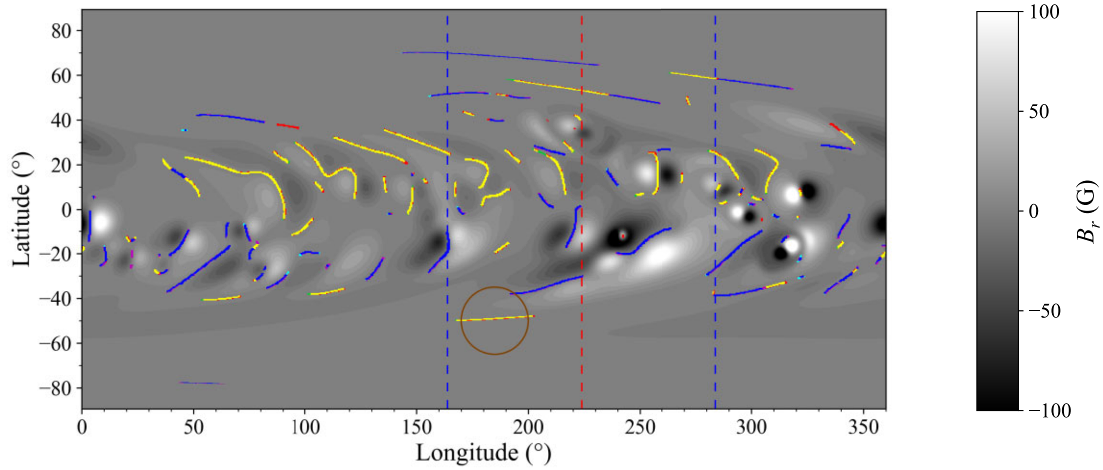

(j) 15 January.

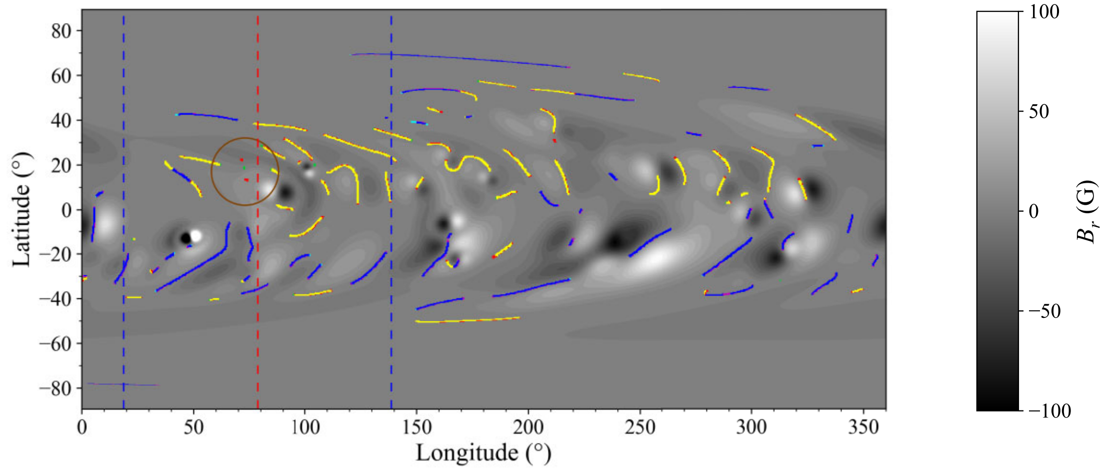

(k) 26 January.

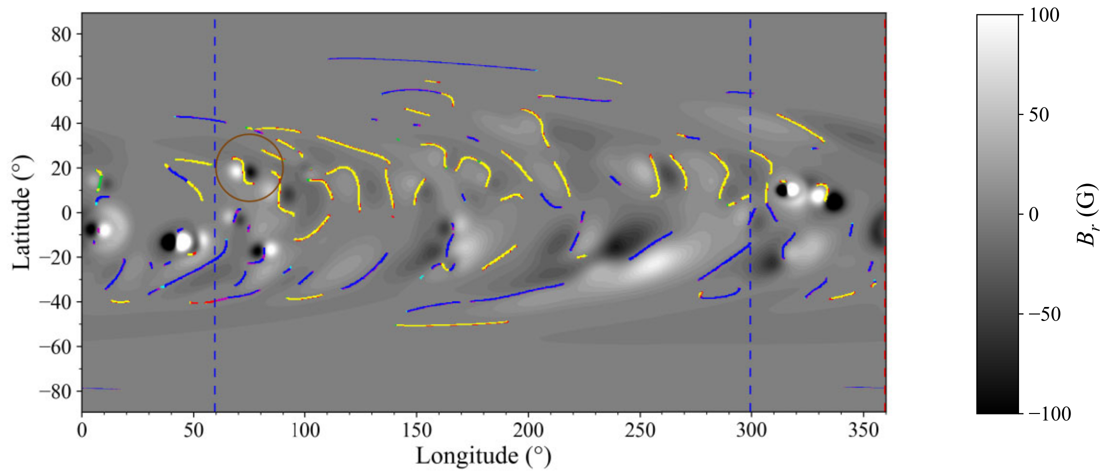

(l) 1 February.

Figure 9. *– continued*

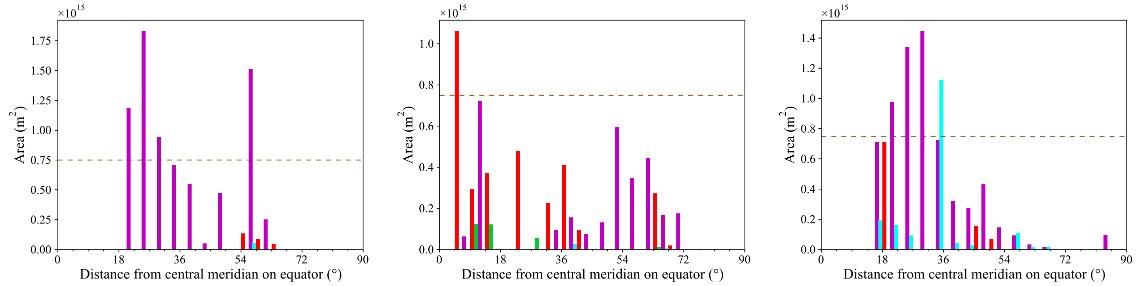

(a) Distances to points on 10 November. (b) Distances to points on 25 November. (c) Distances to points on 28 March.

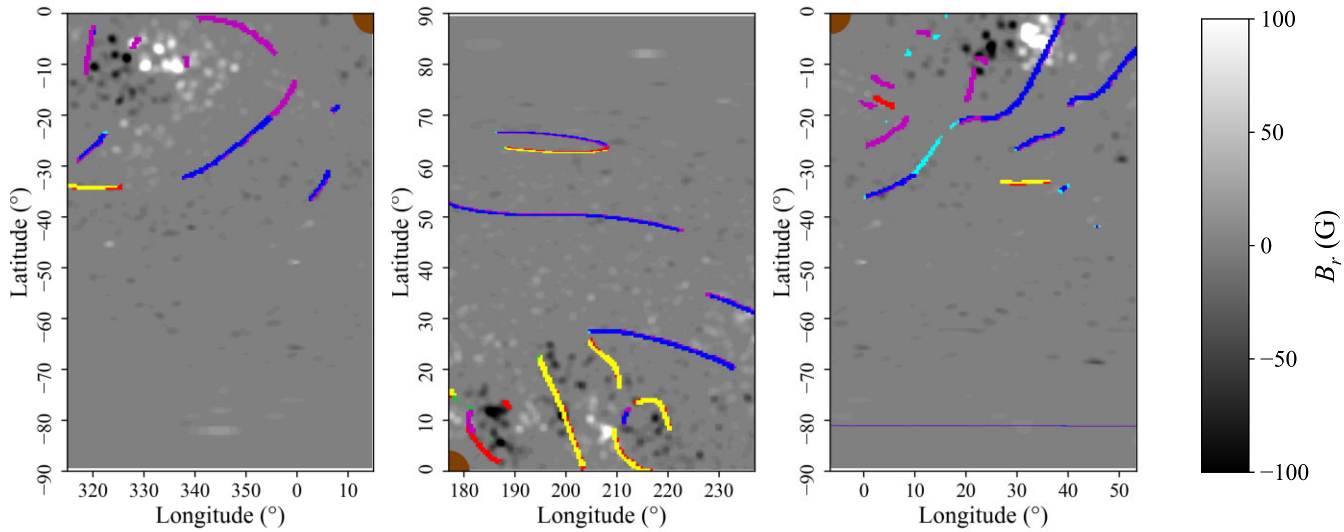

(d) Plots of skew on 10 November. (e) Plots of skew on 25 November. (f) Plots of skew on 28 March.

Figure 10. Points of growing or falling skew in the field of view and their position relative to a reference point at the intersection of the central meridian with the equator. In (a), (b), and (c), histograms show the distances of pixels where skew falls in several of the categories in Table 1 from the reference point, each represented by the bars of the corresponding colour. In (d), (e), and (f), skew above PILs is coloured in accord with Table 1, superimposed on top of maps of the radial magnetic field, drawn according to the scheme used in Fig. 2, with the reference point marked in brown. As in Fig. 2(c), sections of PILs where skew remains below 70° are omitted, for clarity of the remaining features. In (a), (b), and (c), the dashed brown indicates a threshold on area of 7.5×10^4 m^2. In (a) and (d) are skewed locations to the south left of the reference point on November 10, in (b) and (e) cells to the north left on December 14, and in (c) and (f) cells to the south right on March 28. Here, the case with bipolar regions inserted with $\beta = \mp 0.4$, according to the sign of latitude, in order to match the observed preference in helicity, is analysed.

of solar rotation. By the end of September, the hemispheric pattern of predominantly dextral skew (yellow) in the Northern hemisphere, and sinistral (blue) in the Southern, has been established. For the remainder of the simulation, this pattern will persist.

In October, skew evolves, but predominantly through change in existing structures that have appeared over the first rotation. For PILs spanning an extended range in latitude, differential rotation acts upon parts at different latitudes at different rates, and this shear elongates them, such that skew grows in spatial extent. On October 13 (Fig. 9e), another noteworthy example lies at (35°, 45°): a flux rope of dextral skew is seen in the middle of an interval of several days during which it is lengthened by differential rotation. At (55°, 65°), another flux rope is undergoing a similar process, and is already visibly longer than when it originated on September 13 at (120°, 65°) (Fig. 9b). The growth of this strong skew is, by its nature, incremental and, consequently, the majority occurs on the far side of the Sun.

By the start of November (Fig. 9f), the system has sufficiently evolved as to be considered relatively independent of its initial state. From this point onwards, large-scale features dominate the distribution of strong skew. Large features of strong skew generally form mostly or entirely on the far side of the Sun, and then come into view, as opposed to forming while visible on the Earth-facing side. This is a consequence of inserting new flux in the form of bipolar regions only on the near side of the Sun. For instance, one such feature originates in a wisp of growing dextral skew (yellow and red) on November 1 (Fig. 10c) around (90°, −35°), which is then within the field of view visible from Earth. However, this initially tenuous structure has rotated out of the field of view by the time that it has become as a major feature of strong skew at (90°, −40°), as seen on November 16 (Fig. 9g). Most of its evolution to achieve such an elongated form takes place on the far side of the Sun and consists of slow, incremental expansion of the area of strong skew.

Similarly, the very pronounced extent of strong dextral skew (yellow) stretching from (280°, 40°) to (315°, 10°) (Fig. 9f), which is outside the field of view from Earth, enters the field of view around November 11. On the same day, the emergence of a bipolar region in the Southern hemisphere at (309°, −12°) introduces a short PIL, along which sinistral skew is greater than 70° at a small point in the centre. After rotating out of the field of view, this region evolves, and, when it re-enters, a much longer and broader flux rope has formed (December 8; Fig. 9h) at (310°, −10°).

On December 23, the bipolar region responsible for the flux distribution discussed in Section 4 and in the context of Fig. 8(b) emerges. When it does so, it is located at (121°, 9°). On the preceding day, that location is on the edge of the field of view, 60° left of central meridian. On emergence, a new PIL is created between the positive and negative photospheric polarities. Associated with that inversion line, dextral skew is present, but not yet above 70° (and thus not visible in the coloured categories of Fig. 9, which exclude $|\gamma| < 70°$). Over time, as this feature of dextral skew rotates over the solar disc, γ will progressively grow to be above 70° at points above the inversion line. As this occurs, strong dextral skew (yellow) is seen along a progressively longer section of the PIL, producing a progressively larger, more coherent structure. Twelve days after the emergence, by then on the far side of the Sun, this is illustrated by the magnetic field on January 4 (Fig. 9i). Around the same location, the bipolar region is still noticeable on the surface, albeit in fainter patches of black and white, associated with magnetic flux much reduced by the action of diffusion. Strong dextral skew is present between these polarities, and extends along an expansive magnetic feature, to (95°, 30°). Since that feature has an area much larger than those around it, it will dominate the total area of strong skew reported in the field of view when it returns to it, giving rise to the periodic behaviour seen in Fig. 8(b).

As in that example, many features of strong skew originate within the field of view and then continue to form on the far side of the Sun. However, some features also originate on the far side, unconnected with the emergence of bipolar regions. On January 4 (Fig. 9i), strong dextral skew grows along a short segment of a PIL in the Southern hemisphere around (190°, −50°), starting completely outside the field of view. When it enters on January 15 (Fig. 9j), it has grown to an established magnetic structure of much more considerable length.

While such instances are rare, one example of strong skew growing to a noticeable extent within the field of view centres around a bipolar region emerging on January 26 at (73°, 17°), creating a short PIL along which dextral skew appears (Fig. 9k). Over the next few days, this broadens and elongates to form the sinuous region of strong skew by February 1, which is the first day after it leaves the field of view (Fig. 9l). On the far side, the growth of this features continues and it produces a very pronounced filament channel, which is explored more closely in Section 7.

Behaviour of this nature is typical of the later stages of the simulations. Where new bipolar regions emerge, short PILs, associated with considerable skew, form very quickly between their polarities, often within a few days of emergence. However, these short locations of strong skew are too small to represent solar filaments or filament channels. On the other hand, lengthier structures, more indicative of larger filaments, are produced over far longer times by the incremental increase of areas of strong skew. Because these protracted intervals can span several Carrington rotations, this fact has a clear implication for what is observable: only small sections of this ongoing process of growth and development occur within the field of view visible from Earth, while most of the process of the production of skew occurs on the far side. This limitation may be partly due to the fact that new bipolar regions can be included only after they are observed on the near side. This produces a selection effect in these data-constrained simulation.

Table 2. Number of features of growing skew detected exceeding a given threshold on area. Statistics are summed over the full duration of the simulation. Two simulations are compared, inserting bipolar regions with no self-twist ($\beta = 0.0$) and with a degree of self-twist reproducing the hemispheric pattern in helicity ($\beta = \mp0.4$). Results for three thresholds are quoted in order to demonstrate the effect of choosing it. Proportions quoted are the fraction of features detected with a given chirality (dextral or sinistral).

Threshold	Case	Dextral		Sinistral		Total
5×10^{14} m^2	$\beta = 0.0$	196	52.4%	178	47.6%	374
	$\beta = \mp0.4$	248	48.2%	266	51.8%	514
7.5×10^{14} m^2	$\beta = 0.0$	66	56.4%	51	43.6%	117
	$\beta = \mp0.4$	82	46.9%	93	53.1%	175
1×10^{15} m^2	$\beta = 0.0$	18	51.4%	17	48.6%	35
	$\beta = \mp0.4$	37	52.8%	33	47.2%	70

6 SYSTEMATICALLY IDENTIFYING LOCAL FEATURES IN WHICH SKEW FORMS

Integrating areas of each category of skew over the whole Sun and over longitudes visible from Earth quantifies the formation of skew and its persistence, both in small isolated points and as part of large magnetic structures. However, it is also useful to consider the formation of strong skew in specific, spatially coherent features, and the locations of these features. In particular, by identifying these locations, magnetic configurations corresponding to filament channels are found, which can subsequently be compared with observations.

As exemplified in Section 5, locations at which skew forms are numerous, but it is beneficial to quantify them. Hence, some automated method for detecting them is useful, in order to study when and where they occur. For that purpose, cells in each snapshot where skew is seen to grow above 70° or fall below 70° within the field of view are selected (namely those in the red, green, purple, and cyan categories of Table 2). Then, these cells are classified according to whether they lie in the Northern or Southern hemisphere, and whether to the left or right of central meridian. Within each of the four quadrants, the distances of the selected cells, in their separate categories, are calculated from the intersection of the central meridian and the equator, which is taken to be a reference point. Those distances are expressed as the angles subtended on the Sun by the linear distances between the selected cells and the reference point. Then, the selected cells, in each category, are binned according to their distance from the reference point, and the sum of the areas of the cells in each bin found, producing histograms for each category of skew and for each quadrant. Where the total area in a given bin exceeds a chosen threshold, this indicates a large group of points of a certain category of skew that are a similar distance from the reference point, which are assumed to be neighbouring each other. That group is taken to be a distinct feature of skew. Each bin is 4.5° wide, which corresponds to an arc around 50 Mm long on the Sun. Hence, a cluster of points associated with a reasonably sized filament could fall within the same bin, and be detected as such. Empirically, a threshold on area of 7.5×10^{14} m^2 was found to be fairly reliable in identifying distinct features.[17] Using this technique, the potential sites for the formation of filament channels on the visible side of the Sun are identified.

Fig. 10 demonstrates representative selected features identified with this method. Histograms (top row) show the distances between the reference point and pixels where the angle of skew grows above

[17] Such an area could represent a filament of length 75 Mm and breadth 10 Mm.

70° or falls below 70°. Each category is represented by bars of the colour specified by Table 1. Maps of the photospheric magnetic field (bottom row) show areas of skew highlighted using the colours of Table 1, in the format of Fig. 2(c), but with the spatial range focused on one quadrant and with the reference point marked in brown. Each column represents a different day, on which some distinct feature of skew is identified. For each day, the quadrant represented is that in which some notable feature occurs. As in Section 5, results here focus upon the simulation in which bipolar regions emerge with $\beta = \mp 0.4$.

On November 10, to the left of central meridian in the Southern hemisphere, the areal threshold (dashed brown) is breached in four bins (Figs 10a), comprising angular distances in the ranges [18°, 22.5°], [22.5°, 27°], [27°, 31.5°], and [54°, 58.5°] from the reference point. Each contains sinistral skew growing to be above 70° (purple), indicating collections of points separated from the reference points by distances in those ranges. Correspondingly, growing skew is seen in four large features, around (355°, −15°), (350°, −5°), (340°, −10°), and (320°, −5°) (Fig. 10d), these locations being, respectively, approximately 20.25°, 24.75°, 29.25°, and 56.25° from the reference point (brown, here in the top-right corner).

On November 25, histograms find two features where skew grows to be strong, in bins centred 6.75° and 24.75° to the north right of the reference point (Figs 10b). A locations of growing dextral skew (red) around (185°, 5°) clearly corresponds to this. It occurs along the PIL separating a recently emerged bipolar region from the ambient field.

Finally, on 28 March, the histograms (Fig. 10c) show that the threshold is exceeded in bins representing clusters of points around 20.25°, 24.75°, 29.25°, and 33.75° to the south right of the reference point. Two neighbouring patches of growing sinistral skew (purple) at (5°, −15°) lie in the range [18°, 22.5] and provide the first cluster. At (5°, −25°), another fragmented sinistral feature provides a rare instance of growing strong skew not obviously connected with an emerging bipolar region. Strong skew at (20°, −15°) along the PIL internal to a bipolar region is responsible for the third and the largest of these features. All of these three are instance of skew, in this case sinistral, becoming stronger and growing above 70°. Reducing sinistral skew, however, located around (15°, −30°) on a segment of a long, existing structure (cyan), constitutes the feature responsible for the final bin in which the threshold is exceeded.

By applying this technique systematically to all snapshots, potential sites for the formation of filaments are identified, as demonstrated by the several examples discussed. In terms of their sizes, their association with emerging flux, and the greater prevalence of strengthening skew over weakening skew, all of these examples are typical of the simulation as a whole. Analysing the local evolution of skew in this way shows three facts. First, the formation of strong skew within the field of view occurs in relatively small pockets. Those larger structures of strong skew, which may give rise to filaments, do not rapidly or instantaneously form in a large cluster of points where skew grows above 70° at once. Rather, only small parts of them are formed at any one time, with skew growing above 70° only at a few points at once, demonstrating that the formation of large-scale structures characterized by strong skew is an incremental process. Secondly, those small locations where skew grows to be above 70° within the field of view are generally associated with the emergence of new flux in the form of new bipolar regions and occur in immediate response to that emergence through the reconfiguration of the coronal field; the longer-term production of skew is not generally visible in the Earth-bound field of view, as it occurs on time-scales longer than the transit time across the solar disc. Thirdly, the removal of strong skew, through the angle of skew falling below 70°, is far less likely to be detected within the field of view than its production, because, as discussed in Section 4, the removal of strong skew takes place through the more rapid process of the eruption of flux ropes, rather than through a gradual reduction of $|\gamma|$ from above 70° to below 70°.

Applying this analysis, all instances in which the area in one bin where skew grows above 70° exceeds the chosen threshold are extracted. Table 2 shows the number of such instances, within the field of view, totalled over the duration of the simulation, comparing cases with $\beta = 0.0$ and with $\beta = \mp 0.4$. Although only examples from the latter are shown in Fig. 10, comparing the statistics for the two cases illustrates the effect of twist. In order to ascertain the significance of the choice of the threshold on area, statistics are provided for thresholds of 5×10^{14} m^2, 7.5×10^{14} m^2, and 1×10^{15} m^2.

In the case with $\beta = \mp 0.4$, the lowest threshold is breached around one and a third times as often as in the case with $\beta = 0.0$. However, as the threshold is increased to the highest value, this increases to a factor of 2. Evidently, the presence of twist makes the production of strong skew more likely, but it brings about a greater enhancement in larger areas of strong skew than in smaller areas.

Similar analysis applies to the chirality of identified features as applies to their number. Greater skew naturally forms on the PILs above newly emerged twisted bipolar regions, and the bipolar regions in this data set are predominantly in the Southern hemisphere, where sinistral skew is typical. Therefore, adding self-twist to emerging flux increases the creation of sinistral skew more than it increases the creation of dextral skew, as was found in Section 5 with respect to Fig. 4. For this reason, the proportion of features that are sinistral increases when inserting twisted bipolar regions (with $\beta = \mp 0.4$) compared with the case with $\beta = 0.0$, for the two lower thresholds, but not for the largest threshold. At the largest threshold, that proportion little changes, since the features of growing skew of largest area are least affect by the skew associated with the small bipolar emergences. Skew directly associated with bipolar emergence is generally small in area and contributes to a general, small-scale level of total skew. Forming larger structures involves more processes and a more complex evolution, which is contingent on more than emergence alone. In particular, small regions of skewed magnetic fields must be free to develop and grow, without being disrupted, such as by the emergence of new flux. Less total flux and fewer bipolar regions emerging in the Northern hemisphere, where dextral skew dominates, allow the development of such structures to continue over longer periods of time and hence for these structures to attain greater areas. As a result, larger features of strong skew are more likely to be dextral than are smaller features.

Analysis of the form in Fig. 10, however, can overlook some subtleties of the structures in which skew arises. Two instances are shown and discussed in Appendix A. In addition, using histograms such as these shows the production of skew within the field of view, but it is also instructive to be able to detect skew outside the field of view. This would make it possible to understand the likelihood of strong skew being produced within the field of view. For these reasons, a subsequent work (hereafter, Paper II) additionally processes cells of growing skew using a clustering algorithm, thereby providing sets of discrete features.

7 CASE STUDY: FILAMENT ON DAY OF ECLIPSE

On 2015 March 20, the day of the solar eclipse, a large filament is seen near central meridian at (100°, 20°). Figs 11, 12, 13, and 14 illustrate this filament on 3 d. Fig. 11 shows maps of the photospheric field on top of which regions of skew are coloured according to the categories of Table 1, in the manner of Fig. 2(c). Fig. 12 shows

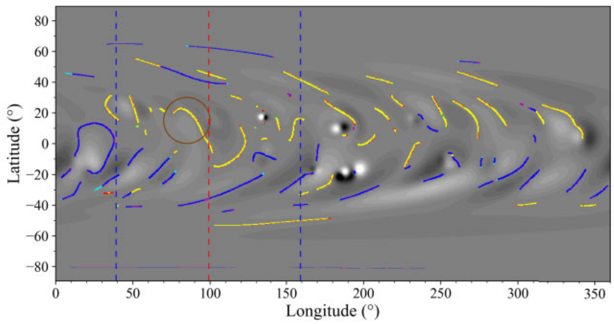

(a) Skew on 20 March.

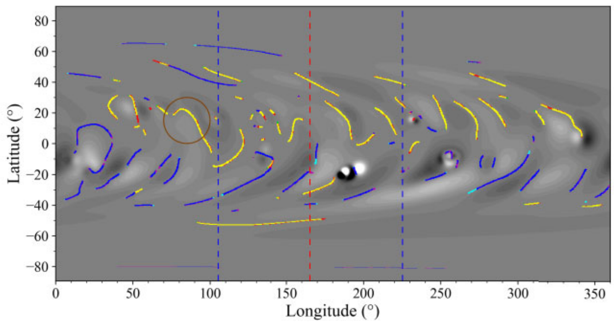

(b) Skew on 15 March.

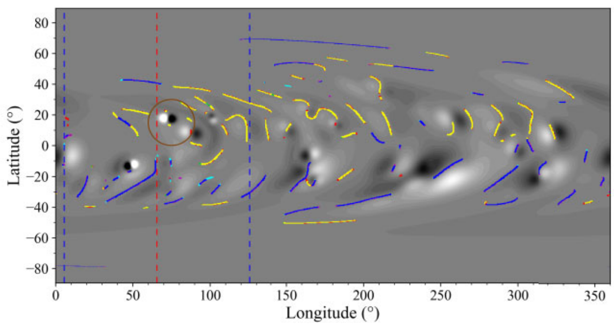

(c) Skew on 27 January.

Figure 11. Large filament discussed in Section 7, which is seen at $(100^\circ, 20^\circ)$ on 2015 March 20, the day of the total solar eclipse, illustrated in the case in which bipolar regions are inserted with $\beta = \mp 0.4$. Areas of skew, shaded according to the scheme given by Table 1, are superimposed upon a map of the photospheric magnetic field, in the manner of Fig. 2(c). For the days represented by these plots, the central meridian is (a) at 99°, (b) at 165°, and (c) at 65°. In brown are circled the different stages of the filament on the several days listed.

observational images of the Sun in Hα from the Big Bear Solar Observatory (BBSO; Leibacher & GONG Project Team 1995). Fig. 13 shows maps of the photospheric field with representative field lines chosen to highlight the structure of the filament, in the format of Fig. 3(a). Fig. 14 shows, in the same format as Fig. 3(b), three-dimensional representations of the Sun in the simulation, showing the photospheric radial magnetic field and, in each panel, the same field lines, as in the corresponding panel of Fig. 13. In each figure, the day represented is (a) March 20, (b) March 15, and (c) January 27.

In Fig. 11(a), the filament is visible as the elongated region of strong dextral skew (yellow) extending from $(80^\circ, 20^\circ)$ to $(110^\circ, -20^\circ)$, crossing central meridian (dashed red; at 99°). In Hα (Fig. 12a), the uppermost parts of the same structure can be seen as the dark thread-like area of absorption lying on central meridian.[18] By plotting field lines around that area (Fig. 13a), the shape of the field in the flux rope is revealed: within it, field lines tend to follow the dominant axial component, along the length of the filament. Those field lines are embedded within an overarching arcade, which can be seen as the field lines crossing above the flux rope. As they do so, these field lines connect opposite polarities in a filament channel on either side of the underlying inversion line. In three dimensions (Fig. 14a), the same field lines show the same structure.

Five days beforehand, the same feature exists, in substantially the same form, before rotation brings it into the field of view. Figs 13(b) and 14(b) show field lines traced from the same starting points as those in Figs 13(a) and 14(a). Comparing with observations showing the Sun five days later reveals the evolution of the field in the intervening period. When it crosses over the limb and on to the solar disc, the flux rope is recognizably the same entity seen on the day of the eclipse (Fig. 11b). Precisely the same is seen in the observation (Fig. 12b):[19] the dense dark filament is pre-existing when it crosses over the limb as the Sun rotates.[20] Between the times at which the filament enters the field of view (March 15) and at which it reaches central meridian (March 20), the configuration of field lines does not significantly change, demonstrating the slow nature of changes in the coronal magnetic field. Field lines in Fig. 13(b) have the same rightwards orientation as they cross the PIL, giving the flux rope the same strong dextral skew and the same shape as it has on March 20. Off the limb, the field lines of the overlying arcade protrude at great heights into the corona, while the filament itself is much more low-lying, nearer to the surface (Fig. 14b). From this, it is clear that this flux rope exists prior to its rotation on to the visible disc.

This filament originates from the emergence on January 26 of a bipolar region at $(73^\circ, 17^\circ)$.[21,22] Each of Figs 11(c), 12(c), 13(c), and 14(c), shows the Sun on the following day. While the new flux in the emergent bipolar region is strong and conspicuous around $(73^\circ, 17^\circ)$ in Fig. 11(c), there is little strong skew associated with it, except in small pockets, where skew has locally formed on the PIL between the two polarities of the new region. Corresponding to the emergence, the Hα observation (Fig. 12c) shows a small white patch of emergent flux stronger than that surrounding it, slightly right of central meridian (circled in brown). Around the nascent bipolar region, the field lines (Fig. 13c) indicate that the field has yet to interact fully and connect fully with the ambient field into which it has emerged. In three dimensions (Fig. 14c), the overlying field straddles the PIL high above the surface, but there are, at this stage, few connections between the field of the emergent bipolar region and the ambient coronal field.

On February 1, the magnetic structure that the new region has created leaves the Earth-bound field of view, containing only a small amount of the strong skew that will characterize the later flux rope, as is seen in Fig. 9(l). Over subsequent days and weeks, this structure connects with the ambient coronal field. As it does so, it progressively

[18]Because the results of the simulation represent noon, but the observation represents a time around 5 h later (the earliest time available), there is a small shift in longitude.

[19]Since no Hα data are available for 2015 March 15, this shows the Sun on 2015 March 16.

[20]As is noticeable in Fig. 12(a), there are two thicker dark segments of the filament between which the filament is thinner. On the limb, the thinner part is, through an effect of projection, slightly more difficult to see, but the two thicker parts are obvious.

[21]Section 5 refers to the same region in relation to Fig. 9(k).

[22]According to the NOAA classification, this is AR 12271.

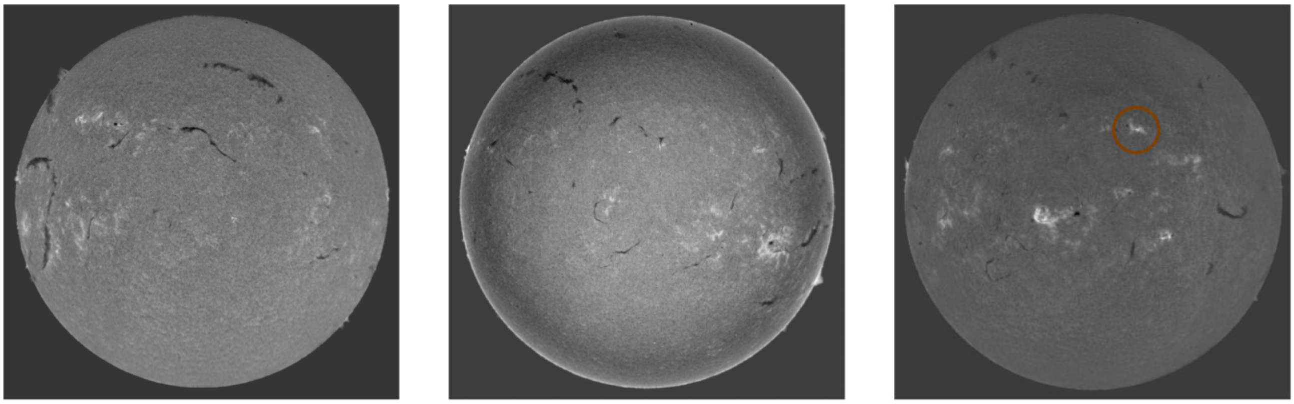

(a) H-α observations on 20 March (at 17:33). (b) H-α observations on 16 March (19:30). (c) H-α observations on 27 January (at 19:52).

Figure 12. Large filament discussed in Section 7, which is seen at (100°, 20°) on 2015 March 20, the day of the total solar eclipse, illustrated in the case where $\beta = \mp 0.4$. Observational images, taken in H α from the BBSO (Leibacher & GONG Project Team 1995), show the state of the Sun, to which the simulation should correspond. In (b), since no H α data are available from the BBSO for March 15, the Sun is shown as observed on 2015 March 16. For the days represented by these plots, the central meridian is (a) at 99°, (b) at 152° (on March 16), and (c) at 65°. In (c), the emergence of the bipolar region with which the filament originates is circled in brown.

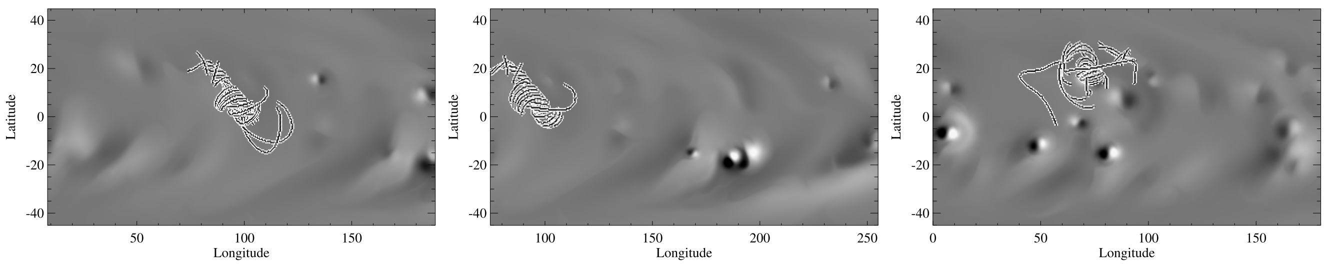

(a) Field lines in simulation on 20 March. (b) Field lines in simulation on 15 March. (c) Field lines in simulation on 27 January.

Figure 13. Large filament discussed in Section 7, which is seen at (100°, 20°) on 2015 March 20, the day of the total solar eclipse, illustrated in the case in which bipolar regions are inserted with $\beta = \mp 0.4$ (Fig. 2c). Field lines, chosen to highlight the filament, are superimposed upon maps of the radial component of the photospheric magnetic field, where white and black represent positive and negative flux, respectively. In (b), the field lines shown are integrated from the same starting points as in (a), such that they are 'the same' ones on the two different days. In each sub-panel, a 180°-wide view is plotted, generally centred on central meridian, similar to what can be seen in observations, as in Fig. 12. In (c), the range shown is [0°, 180°] and thus, unlike (a) and (b), not centred on central meridian, in order to avoid wrapping around 0°. For the days represented by these plots, the central meridian is (a) at 99°, (b) at 165°, and (c) at 65°.

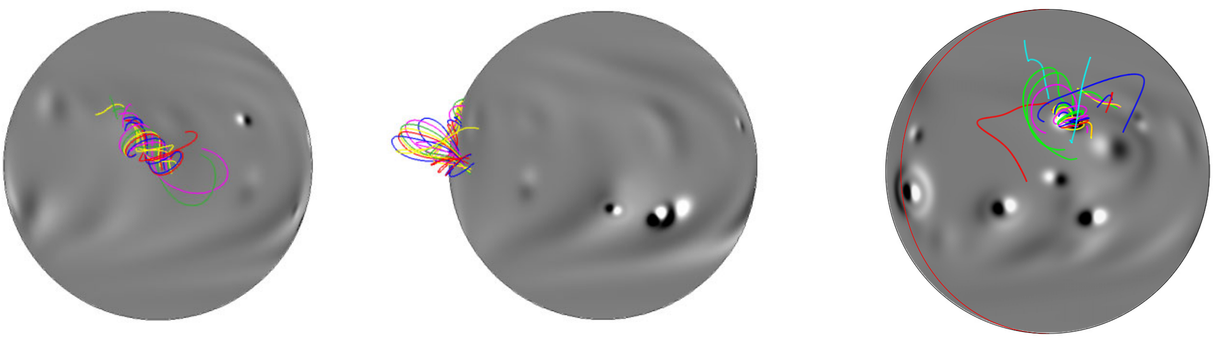

(a) Field lines in simulation on 20 March. (b) Field lines in simulation on 15 March. (c) Field lines in simulation on 27 January.

Figure 14. Large filament discussed in Section 7, which is seen at (100°, 20°) on 2015 March 20, the day of the total solar eclipse, illustrated in the case in which bipolar regions are inserted with $\beta = \mp 0.4$. Here, the filament is illustrated in the case with bipolar regions inserted having $\beta = \mp 0.4$, according to the sign of latitude, in order to match the observed preference in helicity. In (c), the same field lines are shown above a three-dimensional representation of the Sun, likewise shaded according to the photospheric magnetic field. In each panel, the central meridian is in the centre, as in observations, such as those of Fig. 12. For the days represented, the central meridian is (a) at 99°, (b) at 165°, and (c) at 65°.

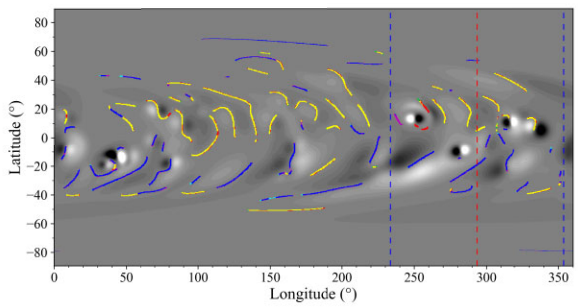

(a) Categories of skew on 6 February.

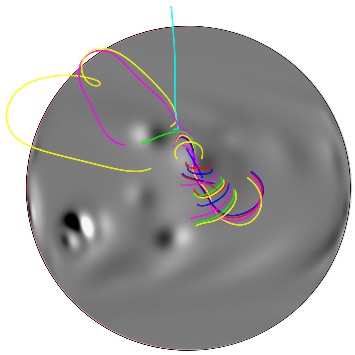

(b) Field lines in simulation on 6 February.

Figure 15. Large filament discussed in Section 7, as it grows on the far side of the Sun on 2015 February 6. Here, the filament is illustrated in the case with bipolar regions inserted having $\beta = \mp 0.4$, according to the sign of latitude, in order to match the observed preference in helicity. In (a) areas of skew, shaded according to the scheme given by Table 1, are superimposed upon a representation of the photospheric magnetic field, in the manner of Fig. 2(c). In (b), the far side of the Sun in the simulation is shown on a three-dimensional model, with field lines traced from the same starting points as those in Fig. 13(a) and (b), and Fig. 14(a) and (b).

lengthens, eventually producing the feature of strong skew visible. This feature subsequently rotates over the limb on March 14, reaching central meridian by March 20. Most of the filament forms through incremental addition to this early structure.

When the associated bipolar region emerges, it does so at a location that, on the day of emergence, is within the field of view. Coincidentally, the emergence of the bipolar region on 2015 January 26 and the filament's visibility on March 20 are separated by 53 d. As this is twice the solar rotation time, the region twice returns to the Earth-facing side of the Sun in this time. During most of that time, however, this region is on the far side of the Sun and thus not visible from Earth. It is when it is on that far side that much of the magnetic configuration that becomes the flux rope forms. Fig. 15 shows maps of the photospheric field on February 6, when that configuration is on the far side. In (a) PILs are superimposed, shaded according to the categories in Table 1. In addition, Fig. 15(b) shows a three-dimensional representation of the Sun, looking at the far side, with field lines traced from the same starting points as those in Fig. 13(a). Around (80°, 15°), and (90°, 5°), the angle of skew increases in very small pockets, from below 70° to above 70° (seen in red in Fig. 15a). Both pockets adjoin a far larger in area where skew remains steadily above 70° (yellow), most of which has formed since the bipolar region in question left the field of view on January 31; these two pockets represent part of the growth of the filament, to the state in which it is seen on March 20. In (b), the axis of the filament is clear, appearing largely as it does much later on March 20 (Fig. 14a). However, the twist is not as strong nor as clearly evident as on the day of the eclipse, indicating that, while the magnetic structure that will support a filament is forming in the filament channel, the field must become more strongly skewed yet. In the slow growth of strong skew, with $|\gamma|$ only growing above 70° in isolated points at any one time, this filament is a good illustration of a general fact, namely that the lengthy process that creates filaments necessarily entails much of that creation occurring on the far side of the Sun.

8 TIME-SCALES FOR PRODUCTION OF STRONG SKEW

Attaining a considerable level of skew, as would be associated with the production of filaments (such as that of Section 7), has consistently been seen to require periods of many days, often comparable with the period of solar rotation. Further to understand this time-scale for the production of strong skew, the cross-correlation between the data representing flux inserted in the form of bipolar regions and the data representing the total area where skew grows above 70°[23] is calculated, as a function of the temporal offset between them. Fig. 16 plots this cross-correlation against the offset in days, for simulations without self-twist ($\beta = 0.0$; Fig. 16a) and with self-twist ($\beta = \mp 0.4$; Fig. 16b). In this context, a peak at a certain number of days offset would reflect the insertion of flux tending to lead to the growth of $|\gamma|$ above 70° this number of days later.

Peaks in the offset between flux being inserted and skew forming occur in both simulations at 0 d and at offsets of around 15 to 18 d. In addition to these, the case with $\beta = \mp 0.4$ also has a small peak at 2 d.

Of these several peaks, that at 0 d is the largest, and is associated with the immediate presence of strong skew on PILs when they form with the emergence of a new bipolar region. With twist in bipolar regions, this skew is greater for $\beta = \mp 0.4$ than for $\beta = 0.0$, as discussed in Section 6, and thus the cross-correlation with zero offset is considerably stronger (around 0.15 compared with around 0.1).

For offsets greater than 0 d, a clear shift in the distribution is brought about by the introduction of twist (in $\beta = \mp 0.4$ compared with $\beta = 0.0$): at larger offset, the correlation is weaker; at smaller offset, less negative, with the additional creation of a positive peak at 4 d. Thus, although skew takes some time to form, this process is slightly hastened by the presence of twist in emerging bipolar regions, with, in particular, an increased propensity to form strong skew after around 4 d. However, it is clear from the graph that far more is still produced after 15 to 18 d, when the bipolar regions have rotated on to the far side of the Sun. Such a delay has consequences for data-driven models that only insert flux on the visible side of the Sun, instead of over the entire surface. Because this delay is longer than the transit time across the solar disc, the locations at which flux is inserted will have rotated out of the Earth-bound field of view and on to the far side of the Sun before strong skew has formed around them.

9 DISCUSSION

Data-constrained magnetofrictional simulations of the solar corona have been performed, seeking to reproduce the coronal evolution from 2014 September 1 to 2015 March 30. Using an observationally

[23] namely, the sum of the red and purple curves in Fig. 5(b).

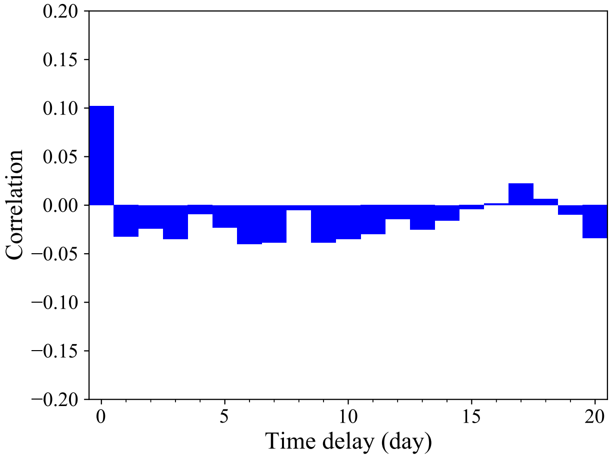

(a) $\beta = 0.0$.

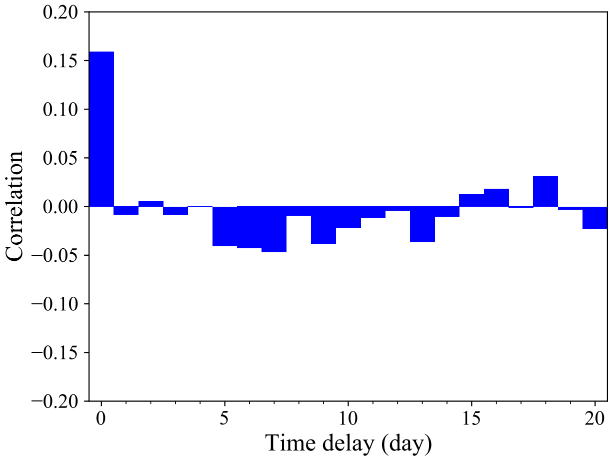

(b) $\beta = \mp 0.4$.

Figure 16. Sample correlation of flux inserted in the form of new bipolar regions and area of growing skew (both dextral and sinistral), plotted against variable temporal offset between them. Results are compared for simulation inserting bipolar regions (a) without self-twist ($\beta = 0.0$) and (b) with self-twist matching the hemispheric pattern in helicity ($\beta = \mp 0.4$).

derived data set, bipolar regions are inserted on the photospheric boundary, simulating the emergence of new flux during that time, in order to model the corona self-consistently.

New techniques have been devised and presented for identifying the formation of magnetic skew within the corona. Using those techniques, the production and persistence of strong magnetic skew, which is characteristic of filaments, have been studied systematically. Particular attention has been paid to where and when strong skew forms, compared with where and when new magnetic bipolar regions emerge, and to the likelihood that skew will form within the field of view visible from Earth.

9.1 Key results

From the work undertaken here, it is evident that

(i) of the strong skew present in the field of view visible from Earth, most is brought in by solar rotation, rather than being created within the field of view (Section 4);

(ii) areas of strong skew originate rapidly in short PILs around new bipolar regions, but most of the area of larger strongly skewed features is added through a protracted process of progressive enlargement in which small areas are incrementally added over long periods of time (Section 5);

(iii) inserting bipolar regions with some degree of self-twist significantly shortens the time needed for the creation of strong skew, but much of that creation still requires more than fifteen days (Section 8);

(iv) the formation and growth of filaments, in which the creation of skew is instrumental, are protracted processes, occurring on time-scales often materially longer than the time-scales associated with transit across the disc (Section 7);

(v) consequently, in a model subject to present observational limitations, in which new magnetic bipolar regions emerge only on the visible side of the Sun, much of the formation of skew inevitably takes place outside the field of view from Earth.

All of these considerations imply a material limitation upon current data-constrained global models of the coronal magnetic field that are limited to using magnetogram data available from the Sun–Earth line. When those simulations are informed by the emergence of flux observed on the Earth-facing side of the Sun, most of the coronal evolution that follows the evolution of that flux will occur on the far side of the Sun, after it has rotated out of view. Conversely, the state of the coronal magnetic field on the near side of the Sun depends upon the state of the photospheric magnetic field on the far side, before it rotates over the limb and into the field of view. Accordingly, simulations relying upon data from such a restricted viewpoint can reproduce that near-side evolution and those near-side structures with only very limited accuracy during their first disc transit.

9.2 Discussion and future work

With the adoption of new techniques for detecting the creation of strong skew, such as is associated with filaments, it is possible systematically to identify and to analyse features in which strong skew is produced. Employing these techniques here demonstrates that skew grows in small distinct features above bipolar regions as they emerge through the photosphere, particularly so above bipolar regions that emerge twisted. However, growing skew is also brought about incrementally, by small areas added on to existing skewed features as they evolve, translate, or elongate. Areas in this latter category appear dispersed over the solar surface and thus the growth of skew appears likewise dispersed both over the Earth-facing and over far-side parts of the Sun. Therefore, although skewed structures have their genesis in PILs rapidly formed above new bipolar regions, wherever those regions emerge, the evolution that leads skewed flux ropes to attain great lengths, such as seen in those supporting filaments, is a much more long-term process, which can last longer than a solar rotation.

Since this study relies upon the identification of PILs and upon the changing skew above PILs, it does not depend on any particular mode of the formation of skew. Therefore, the technique presented here may be universally applied to any other model, as long as the temporal cadence considered is sufficiently high to resolve the evolution of PILs. Hence, the technique could be used for identifying strong skew in models such as those of Amari et al. (2018), Wiegelmann & Neukirch (2003), and Jiang et al. (2016), or in reconstructions derived directly from three-dimensional vector magnetic fields.

One very clear example of this is the filament seen at central meridian on the day of the solar eclipse, discussed in Section 7.

When a modest amount of flux emerges within the field of view, a small amount of strong skew is locally created around it. During the course of two solar rotations, that skewed field grows progressively, as new areas of strong skew are gradually added to it. Most of the flux rope that supports the observed filament is produced in this incremental way. When the solar eclipse occurs on 2015 March 20, it is, once more, within the field of view, and has achieved the elongated structure, which, in addition to the orientation of the field, is suggestive of a filament. Precisely the same is true of most filaments: they are known to persist over very long time-scales, spanning several solar rotations, but, during that time, they are not static, and for much of these lifetimes undergo continual, slow growth, and evolution.

Statistical analysis of the interval between emergence of new flux in the form of bipolar regions and the consequent appearance of strong skew demonstrates a likelihood for untwisted emergent bipolar regions to give rise to strong skew more than two weeks after emergence. Twisted bipolar regions tend to do so after a similar period of time (Section 8). Such time-scales are consistent with the time-scales for flux ropes to form that have previously been reported using a similar global model of the coronal magnetic field (by Mackay & van Ballegooijen 2006a, fig. 4). Accordingly, the emergence of twisted flux is a major factor in the creation of skewed coronal magnetic fields, and thus also of filaments that are supported by them.

Several factors contribute to determining the length of time that this process requires. Much of the coronal evolution is governed by the boundary conditions provided at the photosphere. Each of supergranular diffusion, differential rotation, and meridional flow, on one hand, and the emergence of new flux, on the other, is characterized by its own time-scale, which will influence how rapidly skew is formed. Above the surface, where these processes act, reconnection between newly emerged magnetic flux and the existing magnetic field must take place, and this will introduce its own time-scale.

Whichever factors determine it, that time delay between the emergence of flux and the creation of skew is responsible for one restriction affecting this work, and any similar simulation underpinned by data taken only from an Earth-bound field of view. As a result of this delay, despite originating in flux emerging on the Earth-facing side of the Sun, large features of strong skew – significantly including filaments – will, as a result of solar rotation, no longer be visible from Earth by the time that they have fully formed.[24] As the emergence of new flux can be detected only within the current field of view from Earth, new bipolar regions can only be inserted into such simulations only within that limited window. For that reason, the short-term consequences of bipolar emergence are generally seen within the field of view, and the longer-term consequences occur when the bipolar regions have rotated out of the field of view. Inevitably, this results from the way in which bipolar regions are included, with the limited current field of view. As a result, there is a bias in the model with regard to which aspects of magnetic evolution would be visible from Earth. Accordingly, any model that seeks to follow that evolution most accurately ought to insert new bipolar flux across the entire Sun, without the present restriction of a narrow field of view. In the mean-time, simulations that were able somehow to approximate flux emerging on the far side of the Sun would lessen this bias. Then, it would be possible to investigate the extent to which the narrow field of view for observing bipolar regions determines what simulations find to occur on the Earth-facing side of the Sun and inhibits their short-term accuracy. Nevertheless, following one solar rotation, these simulations can accurately reproduce solar phenomena on the near side of the Sun, as exemplified in Section 7.

Primarily, the focus of this work has been magnetic skew (as defined by Martin & McAllister 1995, 1996). Skew is useful for identifying flux ropes and skew in flux ropes is observationally well constrained (by Leroy et al. 1983, 1984). However, several other quantities can be useful in order to describe the state of the magnetic field. Some of these are also useful indicators of non-potentiality and predictors of the likely occurrence of flares or CMEs. One of these is twist. While high twist has been observed in the corona (Srivastava et al. 2010) and associated with eruptions (James et al. 2018), high twist can be difficult observationally to determine. Another useful indicator is Schrijver's R, which correlates strongly with the likelihood of a flux rope's eruption (Schrijver 2007). Pariat et al. (2017) have proposed an 'eruptivity index' based on the fraction of total relative magnetic helicity contributed by the current-carrying component of the magnetic field. While this itself is not a strong predictor of eruptions (Rice & Yeates 2022), a slight modification of its definition, in respect of the axial component of the magnetic field in flux ropes, yields a potentially strong predictor of eruptivity (Rice & Yeates 2023), which can be useful for applications concerned with space weather. Although beyond the scope of this work, any of these quantities, which can be calculated from a three-dimensional vector magnetic field, could be used in a similar study of how the limited current field of view for magnetographs impairs the ability of data-driven or -constrained simulations to reproduce the formation of non-potential structures on the Earth-facing side of the Sun. In particular, in future studies, the skew computed here could be used to identify local regions of interest within the global field for the computation of these other indices.

In this paper we have discussed the results and limitations of the global non-potential model of Mackay & van Ballegooijen (2006a, b). A key aspect of this model is that magnetic skew and non-potentiality are dynamically built up through the combined processes of large-scale surface motions and flux emergence. Such a time-dependant model is appropriate to model the formation of flux ropes occurring on time-scales comparable with the solar rotation time-scale and across all longitudes and latitudes on the Sun, including the far side. However, as demonstrated in this paper, such a global time-dependent model encounters limitations imposed by the restricted Earth-based field of view presently available to magnetographs, which limits the range of longitudes within which new active regions can be identified and included in the model.

It is, however, important to clarify that several alternative models, such as those of Wiegelmann & Neukirch (2003), Jiang et al. (2016), and Amari et al. (2018), do not suffer the same limitation, since non-potentiality and magnetic skew are included in these models through the incorporation of vector magnetogram data. Through the use of vector magnetogram data, these models are able to capture the non-potential state of the corona, including the presence of flux ropes, directly from observations without the need to simulate its formation over time. Thus, these models do not suffer the same observational bias as the global non-potential model used here. While these techniques are apt for studying the *presence* of strong magnetic skew at a single instance in time, they are not suited to study the *production* of magnetic skew over the entire Sun. This is because vector magnetogram data are currently only systematically available

[24]For example, flux may emerge on the east limb, yet strong skew form several days later on the west limb.

in strong-field regions, and not at high latitudes, nor on the far side of the Sun.

Many different approaches, including time-dependent models that use flux emergence and follow the evolution of the field and static models that are informed by vector magnetograph data, can be used to study the non-potential nature of the corona. Each has its own strengths and weaknesses. Ultimately, future work in modelling of the corona should seek to create hybrid models combining the strengths and mitigating the weaknesses of these existing approaches.

Having here established various means of identifying and quantifying the production and persistence of skew, it will be beneficial to use those techniques in order to quantify this inhibition and to determine how far the narrow field of view impairs models with respect to the production of skew and thus the likely formation of filaments. Paper II does so, by extrapolating the properties of bipolar regions detected within the field of view backwards in time, in order to determine their properties several days earlier, emulating the effect of being able to detect them before they enter the Earth-bound field of view. Then, these extrapolated bipolar regions are inserted into a series of simulations, in order to determine the benefits that would be brought by the ability to detect new flux in an observational window wider than that available at present.

ACKNOWLEDGEMENTS

JR and DHM gratefully acknowledge the financial support of the Science and Technology Facilities Council (STFC) through Consolidated Grants ST/S000402/1 and ST/W001195/1 to the University of St Andrews. LAU was supported by NASA Heliophysics Living With a Star grants NNH16ZDA010N-LWS and NNH18ZDA001N-LWS, and by NASA grant NNH18ZDA001N-DRIVE to the COFFIES DRIVE Centre managed by Stanford University.

For profitable advice regarding indicators of the likelihood of solar eruptions, JR thanks Dr Alexander W. James at University College London and Dr Oliver E. K. Rice at Durham University. For discussion on the analysis of time series, the authors are grateful to Dr Valentin M. Popov.

Numerical simulations discussed here were performed using the Cambridge Service for Data Driven Discovery (CSD3), part of which is operated by the University of Cambridge Research Computing, on behalf of the STFC DiRAC HPC Facility, funded by BEIS via STFC capital grants ST/P002307/1 and ST/R002452/1 and STFC operations grant ST/R00689X/1. DiRAC is part of the National e-Infrastructure.

In the collation and handling of bibliographic references, this research has made use of the Astrophysics Data System (ADS), funded by NASA under Cooperative Agreement 80NSSC21M00561.

DATA AVAILABILITY

The data underlying this article will be shared on reasonable request to the corresponding author.

REFERENCES

Altschuler M. D., Newkirk G., 1969, Sol. Phys., 9, 131
Amari T., Aly J.-J., Canou A., Mikic Z., 2013, A&A, 553, A43
Amari T., Canou A., Aly J.-J., Delyon F., Alauzet F., 2018, Nature, 554, 211
Babcock H. W., Babcock H. D., 1955, ApJ, 121, 349
Bogdan T. J., Low B. C., 1986, ApJ, 306, 271
Contopoulos I., Kalapotharakos C., Georgoulis M. K., 2011, Sol. Phys., 269, 351
Davis W., 1957, The Science News-Letter, 71, 403
Davis W., 1959, The Science News-Letter, 76, 229
DeVore C. R., Sheeley N. R., Jr, Boris J. P., Young T. R., Jr, Harvey K. L., 1985, Sol. Phys., 102, 41
Feng X., Yang L., Xiang C., Jiang C., Ma X., Wu S. T., Zhong D., Zhou Y., 2012, Sol. Phys., 279, 207
Foukal P., 1971, Sol. Phys., 19, 59
Golub L., Pasachoff J. M., 1997, The Solar Corona. Cambridge Univ. Press, Cambridge
Hale G. E., 1931, ApJ, 73, 379
Hapgood M. et al., 2021, Space Weather, 19, e2020SW002593
James A. W., Valori G., Green L. M., Liu Y., Cheung M. C. M., Guo Y., van Driel-Gesztelyi L., 2018, ApJ, 855, L16
Jiang C., Wu S. T., Feng X., Hu Q., 2016, Nat. Commun., 7, 11522
Leibacher J., GONG Project Team, 1995, in Ulrich R. K., Rhodes E. J., Jr, Dappen W., eds, ASP Conf. Ser. Vol. 76, GONG 1994. Helio- and Astro-Seismology from the Earth and Space. Astron. Soc. Pac., San Francisco, p. 381
Leighton R. B., 1964, ApJ, 140, 1547
Leroy J. L., Bommier V., Sahal-Brechot S., 1983, Sol. Phys., 83, 135
Leroy J. L., Bommier V., Sahal-Brechot S., 1984, A&A, 131, 33
Mackay D. H., Gaizauskas V., 2003, Sol. Phys., 216, 121
Mackay D. H., Upton L. A., 2022, ApJ, 939, 9
Mackay D. H., van Ballegooijen A. A., 2005, ApJ, 621, L77
Mackay D. H., van Ballegooijen A. A., 2006a, ApJ, 641, 577
Mackay D. H., van Ballegooijen A. A., 2006b, ApJ, 642, 1193
Mackay D. H., Longbottom A. W., Priest E. R., 1999, Sol. Phys., 185, 87
Mackay D. H., Gaizauskas V., van Ballegooijen A. A., 2000, ApJ, 544, 1122
Mackay D. H., DeVore C. R., Antiochos S. K., 2014, ApJ, 784, 164
Martin S. F., 1998, Sol. Phys., 182, 107
Martin S. F., McAllister A. H., 1995, in AAS/Solar Physics Division Meeting #26. p. 961
Martin S. F., McAllister A. H., 1996, in Uchida Y., Kosugi T., Hudson H. S., eds, Proc. IAU Colloq. 153: Magnetodynamic Phenomena in the Solar Atmosphere – Prototypes of Stellar Magnetic Activity. Kluwer Academic Publishers, Dordrecht, p. 497
Martin S. F., Bilimoria R., Tracadas P. W., 1994, in Rutten R. J., Schrijver C. J., eds, Proc. NATO Advanced Research Workshop, Solar Surface Magnetism. NATO Advanced Study Institute (ASI) Series C: Mathematical and Physical Sciences. Kluwer Academic Publishers, Dordrecht, p. 303
McLean D. J., 1959, Aust. J. Phys., 12, 404
Mikic Z., Linker J. A., 1994, ApJ, 430, 898
Newton H. W., 1943, MNRAS, 103, 244
Pagano P., Mackay D. H., Poedts S., 2013, A&A, 560, A38
Pagano P., Mackay D. H., Poedts S., 2014, A&A, 568, A120
Parenti S., 2014, Liv. Rev. Sol. Phys., 11, 1
Pariat E., Leake J. E., Valori G., Linton M. G., Zuccarello F. P., Dalmasse K., 2017, A&A, 601, A125
Pesnell W. D., Thompson B. J., Chamberlin P. C., 2012, Sol. Phys., 275, 3
Pevtsov A. A., Canfield R. C., Metcalf T. R., 1994, ApJ, 425, L117
Pevtsov A. A., Canfield R. C., Metcalf T. R., 1995, ApJ, 440, L109
Rice O. E. K., Yeates A. R., 2022, Front. Astron. Space Sci., 9, 849135
Rice O. E. K., Yeates A. R., 2023, ApJ, 955, 114
Rust D. M., 1967, ApJ, 150, 313
Sabine E., 1852, Phil. Trans. Roy. Soc. A, 142, 103
Scherrer P. H. et al., 2012, Sol. Phys., 275, 207
Schmidt H. U., 1964, in Hess W. M., ed., The Physics of Solar Flares. National Aeronautics and Space Administration, Washington, DC, p. 107
Schrijver C. J., 2007, ApJ, 655, L117
Schüssler M., Baumann I., 2006, A&A, 459, 945
Snodgrass H. B., 1983, ApJ, 270, 288
Srivastava A. K., Zaqarashvili T. V., Kumar P., Khodachenko M. L., 2010, ApJ, 715, 292
Stenflo J. O., 1990, A&A, 233, 220
Upton L., Hathaway D. H., 2014a, ApJ, 780, 5
Upton L., Hathaway D. H., 2014b, ApJ, 792, 142
van Ballegooijen A. A., Cartledge N. P., Priest E. R., 1998, ApJ, 501, 866
van Ballegooijen A. A., Priest E. R., Mackay D. H., 2000, ApJ, 539, 983

Wiegelmann T., 2007, Sol. Phys., 240, 227
Wiegelmann T., Neukirch T., 2003, Nonlinear Processes Geophys., 10, 313
Yang W. H., Sturrock P. A., Antiochos S. K., 1986, ApJ, 309, 383
Yeates A. R., 2014, Sol. Phys., 289, 631
Yeates A. R., Mackay D. H., 2009, Sol. Phys., 254, 77
Yeates A. R., Mackay D. H., van Ballegooijen A. A., 2007, Sol. Phys., 245, 87
Yeates A. R., Mackay D. H., van Ballegooijen A. A., 2008, Sol. Phys., 247, 103
Yeates A. R., Mackay D. H., van Ballegooijen A. A., Constable J. A., 2010, J. Geophys. Res. A, 115, A09112
Yeates A. R. et al., 2018, Space Sci. Rev., 214, 99
Zirker J. B., Martin S. F., Harvey K., Gaizauskas V., 1997, Sol. Phys., 175, 27

SUPPORTING INFORMATION

Supplementary data are available at *MNRAS* online.

suppl_data

Please note: Oxford University Press is not responsible for the content or functionality of any supporting materials supplied by the authors. Any queries (other than missing material) should be directed to the corresponding author for the article.

APPENDIX A: LIMITATIONS OF USING HISTOGRAMS TO IDENTIFY LOCATIONS OF THE FORMATION OF STRONG MAGNETIC SKEW

Fig. A1 is arranged as is Fig. 10, but with each row containing an example chosen in order to illustrate two of the limitations that can affect this approach to the detection of regions of growing strong magnetic skew.

First, one large feature may be spread across several bins. On November 28, one feature of sinistral skew is found 56.25° to the south left of the reference point (Fig. A1c). Correspondingly, strong sinistral skew prevails over a long stretch of a PIL about (85°, −30°) (Fig. A1c). At the same time, nevertheless, a longer dextral filament is missed, stretching from (80°, −40°) to (100°, −35°): it is so oriented as to span several bins, which include distances between 49.5° and 67.5° from the reference point. All of those bins show large areas of growing dextral skew, but in none of them is the threshold breached (Fig. A1a).

On the other hand, precisely the opposite can also occasionally occur, as happens on December 14, in the quadrant to the north left of the reference point. In the bin [36°, 40.5°], an exceptionally large area of growing dextral skew falls (Fig. A1b), which is explained by two

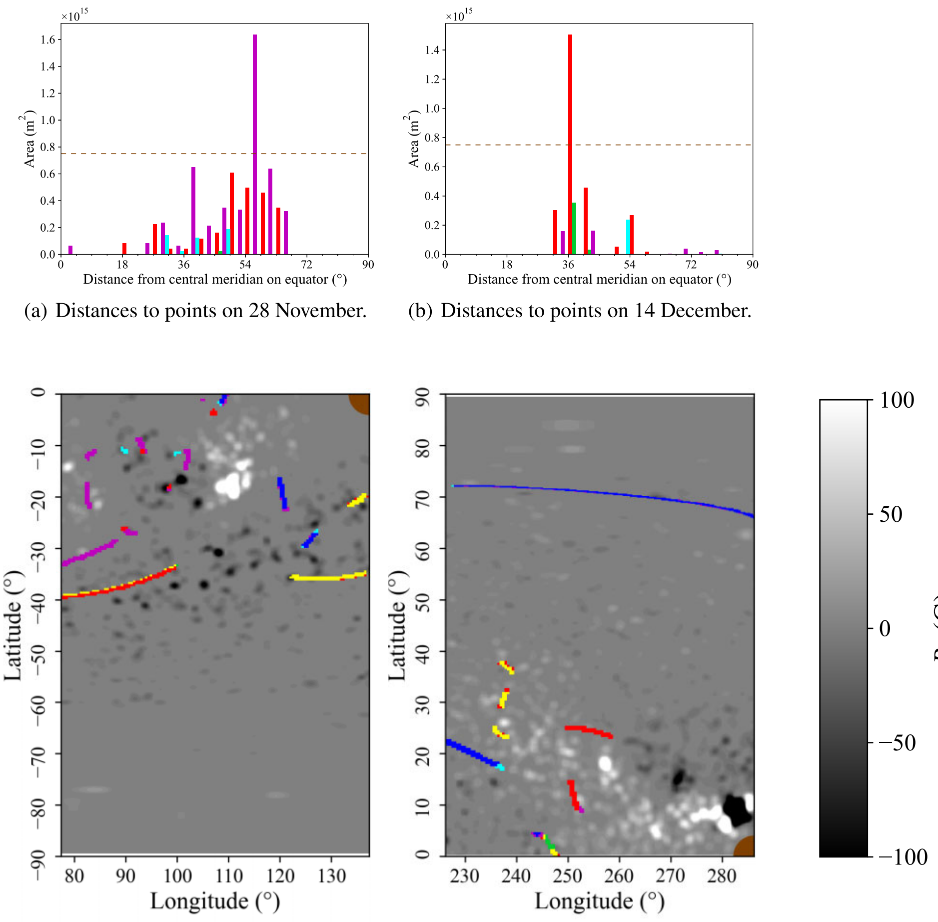

(a) Distances to points on 28 November.
(b) Distances to points on 14 December.
(c) Plots of skew on 28 November.
(d) Plots of skew on 14 December.

Figure A1. Points of strong skew and their position relative to a reference point, in the manner of Fig. 10. Examples shown here are chosen in order to illustrate some caveats affecting such analysis. In (a) and (b), the dashed brown indicates a threshold on area of 7.5×10^4 m^2. In (a) and (c) are skewed locations to the south left on November 28, and in (b) and (d) cells to the north left on December 14. Here, the case with bipolar regions inserted with $\beta = \mp 0.4$, according to the sign of latitude, in order to match the observed preference in helicity, is analysed.

distinct, comparably sized features at (250°, 15°) and at (255°, 25°), the former caused by a newly emerged bipolar region, the latter not (Fig. A1d). Being so close together, these two are registered as a single feature, within one bin.[25]

In these two examples, two opposing limitations on this technique are demonstrated, one mistakenly identifying a potential site for the formation of a filament, the other missing such a site. While insightful therefore there are some caveats when computing the growth of skew within the field of view in this way. Rigorously identifying coherent, distinguishable features requires more than merely finding cells with growing skew that are in a similar direction and at a similar distance from a reference point. It is further necessary that such cells be adjacent to each other, and thus form part of some continuous structure.

[25] Indeed, with each being significant on its own, the combined area in the bin is around twice the threshold.

This paper has been typeset from a TEX/LATEX file prepared by the author.